International Journal of Mechanical Sciences 297–298 (2025) 110349

Contents lists available at ScienceDirect

International Journal of Mechanical Sciences

journal homepage: www.elsevier.com/locate/ijmecsci

Automatic remeshing in limit analysis with deformable polygon discretization

Yiwei Hua *, Gabriele Milani

Department of Architecture, Built Environment and Construction Engineering, Politecnico di Milano, Piazza Leonardo da Vinci 32, Milan 20133, Italy

ARTICLE INFO

Keywords:
Limit analysis
Deformable elements
Interfacial discontinuities
Polygon discretization
Geomechanics
Masonry structures

ABSTRACT

Automatic remeshing holds promise for reducing mesh dependency in numerical simulations. However, its current application in limit analysis primarily relies on triangular meshes. Existing mesh refinement schemes are often not general enough to accommodate complex discretizations. To address this, the paper introduces a dissipation-based automatic remeshing strategy for finite element limit analysis, which supports meshes with arbitrary element shapes and enables interfacial velocity discontinuities and selective refinement. The element deformation is assumed to be homogeneous. The approach is applied to analyze the collapses of the weightless cohesive-frictional strip footing and of a masonry arch bridge interacting with the backfill. The results obtained both indicate the reliability and effectiveness of the proposed remeshing procedure, showing competitive efficiency when compared with a global uniform refinement. Applying remeshing to polygon discretizations is crucial since it can effectively release the locking effect induced by the constant-strain assumption inside the elements, and the converged load prediction can gain precision comparable to the triangular one. Polygon elements exhibit great efficiency in large-scale applications, requiring only 1/5 – 1/2 of processing time when compared with triangular meshes. Regular polygons are more recommended given the lower sensitivity to the initial mesh. The proposed procedure broadens the applicable scenarios of remeshing in limit analysis, providing also a paradigm for mesh refinement in other mesh-based simulations.

1. Introduction

Fast determination of the load-carrying capacity of the system deserves great consideration especially when performing structural safety assessments. Limit analysis is a promising and standard framework that has demonstrated a great edge in that regard, requiring only a few mechanical parameters. In the last century, inspired by finite element analysis, continuous modeling has gained a wide application in limit analysis [1], where discretization is employed to approximate the structural continuum domain, and the prescribed velocity field is assigned for each element. This approach was soon generalized to feature the velocity discontinuities in the continuum [2,3], being more suitable to describe the failure mechanism of the system. Despite the involvement of the discontinuities, the problem can be stated as standard Linear Programming (LP) optimizations on the condition that the associated flow rule holds, whether applying Upper Bound (UB) or Lower Bound (LB) theory (see [2–4]), and robust algorithms to solve these optimizations are accessible thanks to the boom of Operations Research (OR). Typically, the problem can be solved efficiently in a single step even in a large-scale scenario. Recently, this theoretical framework has absorbed more advanced techniques such as the meshless method [5], high-order element [6], nodal smoothing [7], etc., broadening its application to more complicated modeling with reinforcement [8], crack propagations [9,10] or large deformation [11,12]. An important application of this approach in recent decades regards the collapse analysis of masonry systems. Many researchers employed it to understand the behavior at collapse of typical structural elements belonging to masonry historical buildings, such as walls [13], vaults [14,15], or domes [16]. Even the study of the introduction of different strengthening technologies—both innovative and traditional—is possible within limit analysis, adopting some ad-hoc simplified hypotheses [17]. On the other hand, this approach has also gained particular popularity in the geomechanics field, for instance for slope stability problems [18–20] or in soil-structure interaction studies [21,22].

Because of the involvement of the continuum discretization, to investigate the mesh dependence of the results is paramount, an issue which is, however, basically left in the background for most of the

* Corresponding author.
E-mail address: yiwei.hua@polimi.it (Y. Hua).

https://doi.org/10.1016/j.ijmecsci.2025.110349
Received 5 January 2025; Received in revised form 3 May 2025; Accepted 4 May 2025
Available online 5 May 2025

literature (see [11,12] as an example). Performing automatic remeshing could be more efficient in reducing mesh dependence than the global refinement adopted in the traditional mesh sensitivity analysis. This technique has been widely employed in many mesh-based analyses [23,24], particularly useful when the problem involves cracking [25,26] or high-rate large distortion [27]. Those advances have been gradually migrated to the applications of finite element limit analysis. Nevertheless, remeshing proposed in recent decades for limit analysis has proved to be suitable for triangular meshes with regular geometric domains (e.g., [28]). However, its robustness in general and practical scenarios requires more demonstrations from application studies. In these contributions, the element selection naturally refers to a dissipation- or deformation-based indicator, given that the error-based estimator commonly used in elastic cases may not be accessible in plastic limit analysis, and the bulks with higher dissipation or deformation will be chopped priorly. A straightforward idea for the selection is to consider the first n bulks with higher dissipation [29,30], whereas a more precise procedure could be including the elements into the refinement set in descending order of dissipation, until the sum of the dissipation in the set exceeds a given threshold [31–33], which is typically a percentage of the total system dissipation. Another interesting indicator for the remeshing is represented by the gap between lower- and upper-bound solutions in terms of collapse multiplier [34–36]. However, the computational cost of such analysis could represent an issue, because both lower- and upper-bound optimizations should be solved in each round of the refinement, doubling the effort. Besides the element selection, the element refinement scheme adopted in the remeshing procedure lacks further discussions and comparative studies. Uniform subdivision of the element is widely adopted in the h-refinement strategy, whereas it could bring about a local explosion of the element amount (see [37,38]). Several works also used the centroid division, but moving the integration points accordingly, to improve the computational precision of the element energy (e.g., [31]). Adaptive adjustment of the discretization is necessary for better accuracy in more complicated cases. Prior knowledge of the collapse mechanism is sometimes required though, to assign target domains proper refinement schemes [39,40]. More automatically, a direct optimization of the global mesh is possible. For instance, Milani and Lourenço have presented in [41] a Sequential Linear Programming (SLP) scheme of mesh adaptation, with a discretization constituted by Bézier elements, where the coordinates of the control points were included as unknowns for optimization. In another cluster of contributions, a global error indicator has been proposed to measure the deviation induced by the discrete approximation (see [42,43]). Through minimizing this indicator, an adaptive update of the mesh can then be completed through a heuristic search or an optimization algorithm. Nevertheless, as expected, such adaptive and global manipulation on the mesh could sometimes be time-consuming.

Besides the popular triangular mesh, we have also proposed another option for discretization in the previous paper [44]: a constant-strain polygon element. It has demonstrated great edges in modeling complex slip-lines, improving also the flexibility of the mesh configuration. However, the interior locking effect induced by the constant-strain assumption could make the collapse load highly overestimated in some cases [44]. Applying the remeshing procedure could be more essential in this scenario for it can theoretically release the locking effect. Since the triangular elements are less suffering from locking, particularly when the interfacial discontinuities are allowed, we can conduct the remeshing to iteratively split polygon bulks with large dissipation into small triangles. Eventually, the global locking of the system should gradually be precluded and the load prediction should converge to a precise level. Unfortunately, available refinement for the polygon bulks is quite limited in the current literature. We only note several applications of uniform subdivision or simple triangularization directly migrated from the triangular case [23,45–47].

This paper will establish a more solid and automatic remeshing procedure for limit analysis, compatible with general polygon discretizations. The structure of this paper will be organized as follows: in Section 2, after the brief recall of the limit analysis formulation of the constant-strain polygon, we will set out to establish the iterative remeshing procedure, where the high-dissipated elements will be iteratively refined. We will propose specific refinement for polygon bulks and triangular elements. Section 3 will take the weightless cohesive-frictional strip footing problem as a benchmark for comparative studies to investigate the underlying improvement of the procedure configuration. We will compare the effect of different refinements for the triangles, followed by configuration comparisons when applying polygon discretizations, through which the optimal remeshing configuration will be concluded. Section 4 will head to a more practical problem: the collapse of Prestwood Bridge. The remeshing approach will be applied to the backfill region of the bridge. In this case study, the performance of triangular and polygon discretizations combined with local remeshing will be understood, with an additional contrast to the classic global refinement. The paper closes with a discussion of the results and several concluding remarks in Sections 5 and 6, respectively.

2. Methodology

Below we will elaborate on establishing the automatic remeshing procedure for continuous limit analysis modeling. We first recall briefly the governing formulation of the homogeneous deformable element (proposed in [44]). The remeshing procedure applying to general discretization will then be proposed based on iteratively solving this formulation. Note that in the paper we enable the velocity discontinuities across the element edges for a more general purpose, since as pointed out by Sloan and Kleeman [3], the case without interfacial discontinuities can be conveniently realized through an extra constraint of zero interfacial plastic multiplier. Furthermore, some papers have reported the merit of involving velocity jumps, which usually bring about a more conservative prediction [3,48], while the collapse mechanism may sometimes deviate if the discontinuities are not aligned with the actual slip-lines. We will demonstrate and discuss this aspect in the result section.

2.1. Brief recall of limit analysis theory for homogeneous deformable element

The limit analysis formulation will be established based on the Upper Bound (UB) theorem, namely from the kinematic point of view. Duality theorem in the UB optimization can get access to the static solutions (e.g. interfacial resultants and element stresses). In this theory, the element shape is not restricted to be triangular. They can be arbitrary polygon shapes for a more complex discretization purpose.

$$\mathbf{u}^i(\mathbf{r}^i) := \mathbf{u}^i_{\mathscr{R}}(\mathbf{r}^i) + \mathbf{u}^i_{\mathscr{E}}(\mathbf{r}^i) = \mathbf{H}^i_{\mathscr{P}}(\mathbf{r}^i)\mathbf{u}^i_{\mathscr{P}} \tag{1}$$

$$\mathbf{H}^i_{\mathscr{P}}(\mathbf{r}^i) = \begin{bmatrix} 1 & 0 & -(y-\overline{y}^i) & x-\overline{x}^i & 0 & y-\overline{y}^i \\ 0 & 1 & (x-\overline{x}^i) & 0 & y-\overline{y}^i & x-\overline{x}^i \end{bmatrix}$$
$$\mathbf{u}^i_{\mathscr{P}} = \begin{bmatrix} u^i_c & v^i_c & \omega^i_c & \varepsilon^i_x & \varepsilon^i_y & \varepsilon^i_{xy} \end{bmatrix}^T \tag{2}$$
$$\mathbf{r}^i := \begin{bmatrix} x-\overline{x}^i & y-\overline{y}^i \end{bmatrix}^T, \overline{x}^i := \frac{1}{N}\sum_{k=1}^{N} x^i_k, \overline{y}^i := \frac{1}{N}\sum_{k=1}^{N} y^i_k$$

We start with the deduction of compatibility for the element with a general polygon shape. Due to assuming the homogeneous deformation for the element (i.e. constant-strain field), its velocity field $\mathbf{u}^i(\mathbf{r}^i)$ can be explicitly represented as a superposition of rigid body motion $\mathbf{u}^i_{\mathscr{R}}(\mathbf{r}^i)$ and constant-strain mode $\mathbf{u}^i_{\mathscr{E}}(\mathbf{r}^i)$ (Eq. (1)). We introduce the mapping matrix $\mathbf{H}_{\mathscr{P}}$ to project the centroid unknowns $\mathbf{u}_{\mathscr{P}}$ to the field of the entire bulk (Eq. (2)).

Then, the computation of the interfacial discontinuities is straightforward. We assign each interface j two nodes overlapped by the

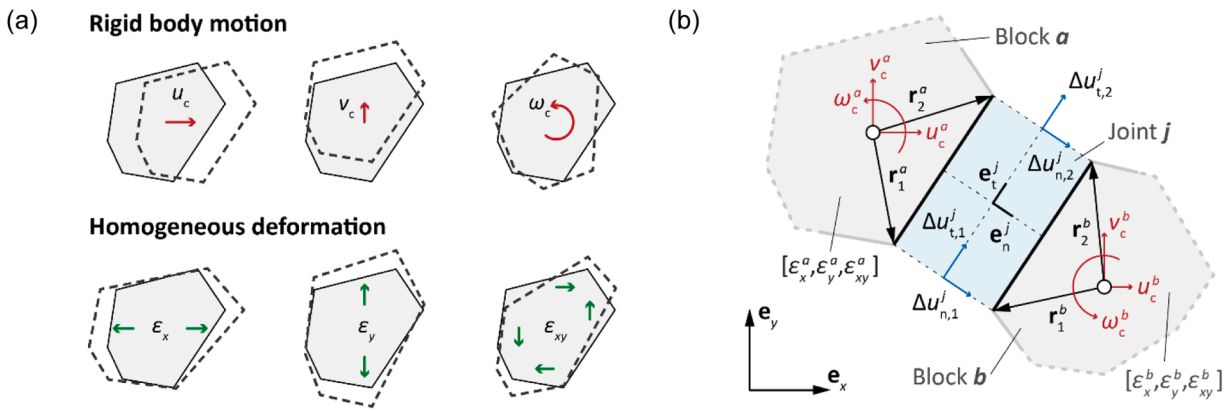

Fig. 1. Compatibility condition of the constant-strain polygon. (a) Definition of rigid body and homogeneous deformation modes. (b) Joint j with two adjacent polygon bulks a and b, interface compatibility.

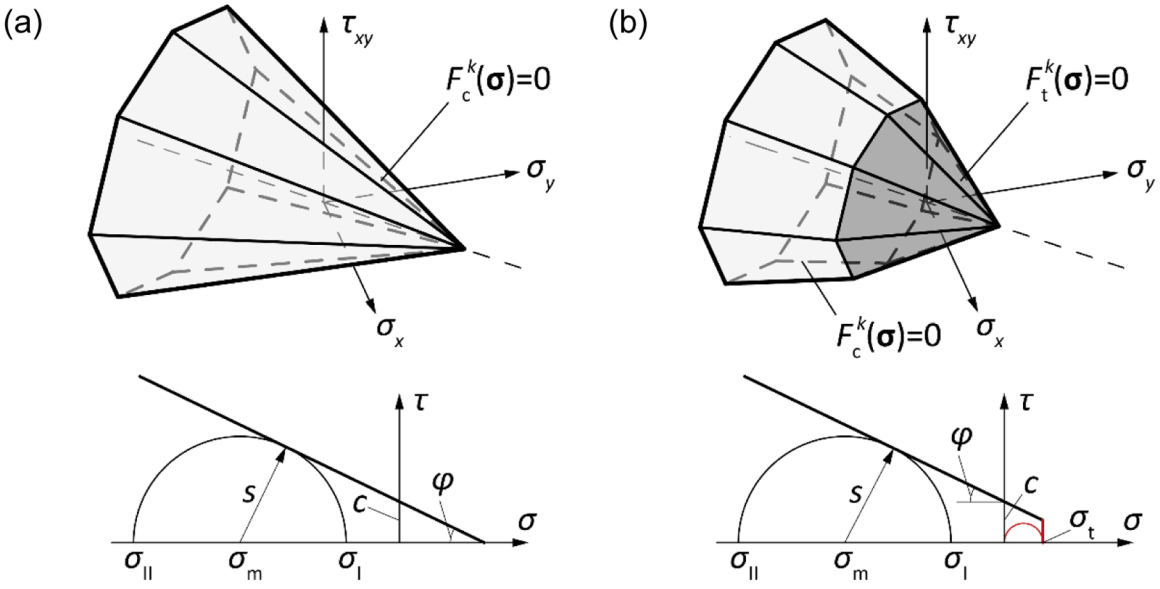

Fig. 2. Limit surface of 2D Mohr-Coulomb friction model with linearization. (a) No tension cutoff. (b) With tension cutoff.

adjacent bulks (Fig. 1) and each node has normal and tangential discontinuities. Namely, we need four freedoms (denoted as $\Delta u^j_{\mathrm{n},1}$, $\Delta u^j_{\mathrm{t},1}$, $\Delta u^j_{\mathrm{n},2}$, $\Delta u^j_{\mathrm{t},2}$) for each interface. These unknowns can be calculated by projecting the velocity difference of each overlapped node pair to the local interfacial frame (Eq. (3a)). Eventually after the assembling, we can obtain a relation between the interfacial discontinuous $\mathbf{q}$ and the element unknowns $\mathbf{u}_{\mathscr{P}}$, associated by the compatibility matrix $\mathbf{A}^T_{\mathscr{P}}$ (Eq. (3b), first equation, left-hand side). The right-hand side of the compatibility equality is the computation of the same velocity jump $\mathbf{q}$ but from the plasticity multiplier $\mathbf{p}$, according to the associated flow rule. Here, we employ the well-acknowledged Mohr-Columb friction model [49], which can be represented by a linear operator $\mathbf{N}^T$ (see [50,51] for details). The dissipation of the interfaces P^{C}_D can also be computed from the plasticity multiplier $\mathbf{p}$ and interfacial cohesion vector $\mathbf{c}_0$ (see the second equality in Eq. (3b)).

$$\mathbf{A}^i_{j,\mathscr{P}} = \begin{bmatrix} \mathbf{Q}_j \mathbf{H}^i_{\mathscr{P}}(\mathbf{r}^i_1) \\ \mathbf{Q}_j \mathbf{H}^i_{\mathscr{P}}(\mathbf{r}^i_2) \end{bmatrix}^T, \mathbf{Q}_j = \begin{bmatrix} \mathbf{e}^j_{\mathrm{n}} & \mathbf{e}^j_{\mathrm{t}} \end{bmatrix}^T, i = a, b \tag{3a}$$

$$\mathbf{A}^T_{\mathscr{P}} \mathbf{u}_{\mathscr{P}} = \mathbf{N}^T \mathbf{p}, \mathbf{p} \geq 0, P^{\mathrm{C}}_D = \mathbf{c}^T_0 \mathbf{p} \tag{3b}$$

$$\begin{aligned} F_{\mathrm{c}}(\sigma,\tau) = c - \sigma\tan\varphi - \tau = 0 &\xrightarrow{\text{to normal stress space}} F_{\mathrm{c}}(\boldsymbol{\sigma}) = 0 \\ F_{\mathrm{c}}(\boldsymbol{\sigma}) = \sqrt{(\sigma_x - \sigma_y)^2 + 4\tau^2_{xy}} + (\sigma_x + \sigma_y)\sin\varphi - 2c\cos\varphi & \end{aligned} \tag{4a}$$

$$\begin{aligned} F_{\mathrm{t}}(\sigma,\tau) = \sigma_{\mathrm{I}} - \sigma_{\mathrm{t}} = 0 &\xrightarrow{\text{to normal stress space}} F_{\mathrm{t}}(\boldsymbol{\sigma}) = 0 \\ F_{\mathrm{t}}(\boldsymbol{\sigma}) = \sqrt{(\sigma_x - \sigma_y)^2 + 4\tau^2_{xy}} + (\sigma_x + \sigma_y) - 2\sigma_{\mathrm{t}} & \end{aligned} \tag{4b}$$

$$\begin{aligned} &\sigma = \sigma_{\mathrm{m}} + s\sin\varphi, \tau = s\cos\varphi, \sigma_{\mathrm{I}} = \sigma_{\mathrm{m}} + s, \sigma_{\mathrm{II}} = \sigma_{\mathrm{m}} - s \\ &\sigma_{\mathrm{m}} = \frac{1}{2}(\sigma_x + \sigma_y), s = \frac{1}{2}\sqrt{(\sigma_x - \sigma_y)^2 + 4\tau^2_{xy}} \end{aligned} \tag{4c}$$

The constitutive model for the element plasticity is again the standard Mohr-Coulomb relation but with linearization [3,52] (Fig. 2a). The yield surface is analytically defined in Eq. (4a) when F_{c} is set equal to zero, which indicates that all the allowed stress states are bounded by the cone defined by frictional angle φ and cohesion c (see Fig. 2a). Deducing backward the normal stress space (using Eq. (4c)), the static-allowed domain is a quadratic cone. We use several linear planes to approximate the real limit surface to avoid the inclusion of nonlinearity. Eq. (5d) gives the coefficients (A^k_{c}, B^k_{c}, and C^k_{c}) of the planes for the p-plane linearization (k denotes the coefficients for the kth plane). We can also adopt a constitutive relation equipped with an additional

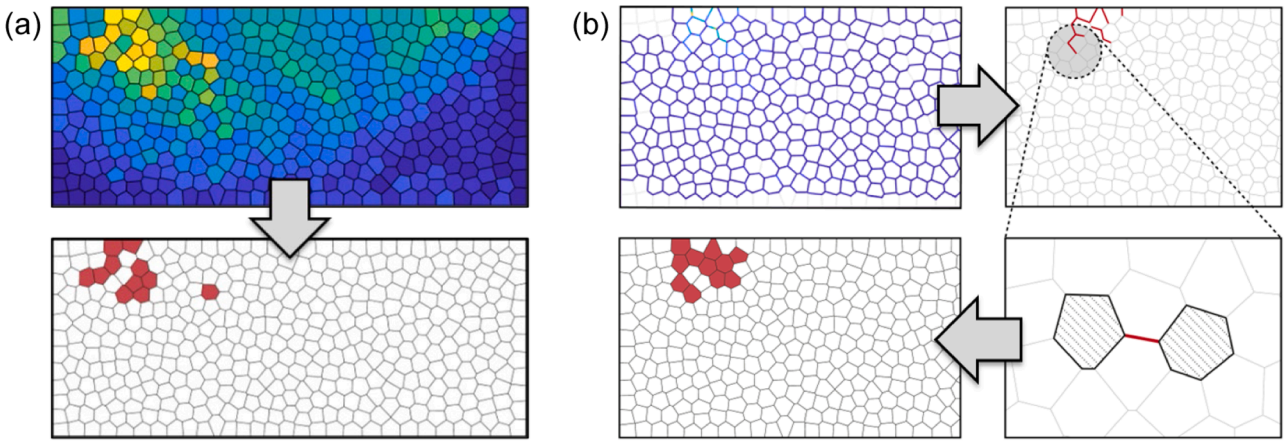

Fig. 3. Element selection criterion in each iteration of automatic remeshing. (a) Based on element dissipation. (b) Based on interfacial dissipation.

tension cutoff in the σ-τ space, defined by the tension limit σ_t (Fig. 2b, Eq. (4b)), which enables an extra conic constraint to the normal stress space. Eq. (5d) gives the corresponding linearizing coefficients (A_t^k, B_t^k, and C_t^k) [53,54]. After the implementation of the linearization, both element constitutive models (with or without tension cutoff) can be unified as the same linear constraint (Eq. (5a)), where the constitutive operator $\mathbf{M}$ consists of all the coefficients of linearization (Eq. (5c)). The cohesion force vector $\mathbf{c}_i$ contains the integral of the cohesion stress c or cutoff stress σ_t over the element volume (Eq. (5b)). Remark that this constitutive law can also be stated as a conic constraint without approximation. The limit analysis formulation will correspondingly become a Second-Order Conic Programming (SOCP). Although the SOCP solving algorithm has become mature in recent decades, this paper still employs linearized constitutive relations for the sake of simplicity.

$$\mathbf{M}\widetilde{\boldsymbol{\sigma}} - \mathbf{z}_1 = \mathbf{c}_1, \mathbf{z}_1 \le 0, \widetilde{\boldsymbol{\sigma}}_i := |E_i| d \begin{bmatrix} \sigma_x^i & \sigma_y^i & 2\tau_{xy}^i \end{bmatrix}^T \tag{5a}$$

$$\begin{aligned} &\mathbf{c}_{1,i} = |E_i| d \begin{bmatrix} 2c\cos\varphi & 2c\cos\varphi & \cdots & 2c\cos\varphi \end{bmatrix}^T \\ &\text{or} \quad \mathbf{c}_{1,i} = |E_i| d \begin{bmatrix} 2c\cos\varphi & \cdots & 2c\cos\varphi & 2\sigma_t & \cdots & 2\sigma_t \end{bmatrix}^T \end{aligned} \tag{5b}$$

$$\mathbf{M}_i = \begin{bmatrix} A_c^1 & A_c^2 & \cdots & A_c^p \\ B_c^1 & B_c^2 & \cdots & B_c^p \\ C_c^1 & C_c^2 & \cdots & C_c^p \end{bmatrix}^T \text{ or } \mathbf{M}_i = \begin{bmatrix} A_c^1 & \cdots & A_c^p & A_t^1 & \cdots & A_t^p \\ B_c^1 & \cdots & B_c^p & B_t^1 & \cdots & B_t^p \\ C_c^1 & \cdots & C_c^p & C_t^1 & \cdots & C_t^p \end{bmatrix}^T \tag{5c}$$

$$\begin{cases} A_c^k = \sin\varphi + \cos a_k \\ B_c^k = \sin\varphi - \cos a_k \\ C_c^k = \sin a_k \end{cases}, \begin{cases} A_t^k = 1 + \cos a_k \\ B_t^k = 1 - \cos a_k \\ C_t^k = \sin a_k \end{cases}, \; a_k = 2\pi k \Big/ p, \; k = 1, 2, \cdots, p \tag{5d}$$

The plasticity flow of the element is again associated with the constitutive, which can be represented by $\mathbf{M}^T$ (left-hand side of Eq. (6)). The right-hand side of Eq. (6) is the compatibility of element deformation, deducing the deformation description from centroid unknowns of the bulk. In this case, the deformation compatibility mapping is a simple boolean selection matrix to extract the constant strain variables from the global unknown list. The element dissipation term shares the same representation as the interfacial one (given in the third equality of Eq. (6)).

$$\mathbf{M}^T\boldsymbol{\lambda} = \mathbf{B}^T\mathbf{u}_{\mathscr{P}}, \mathbf{B}_i = \begin{bmatrix} \mathbf{O}_{3\times3} & \mathbf{I}_{3\times3} \end{bmatrix}^T, \boldsymbol{\lambda} \ge 0, P_D^{\mathrm{E}} = \mathbf{c}_1^T\boldsymbol{\lambda} \tag{6}$$

$$\begin{aligned} \min \quad & -\mathbf{f}_D^T\mathbf{u}_{\mathscr{P}} + \mathbf{c}_0^T\mathbf{p} + \mathbf{c}_1^T\boldsymbol{\lambda} \\ s.\,t. \quad & \mathbf{f}_L^T\mathbf{u}_{\mathscr{P}} = 1 \\ & \mathbf{A}_{\mathscr{P}}^T\mathbf{u}_{\mathscr{P}} = \mathbf{N}^T\mathbf{p}, \; \mathbf{p} \ge 0 \\ & \mathbf{M}^T\boldsymbol{\lambda} = \mathbf{B}^T\mathbf{u}_{\mathscr{P}}, \; \boldsymbol{\lambda} \ge 0 \end{aligned} \tag{7}$$

$$\begin{aligned} \max \quad & \alpha \\ s.\,t. \quad & \mathbf{A}_{\mathscr{P}}\mathbf{x} + \mathbf{B}\widetilde{\boldsymbol{\sigma}} = \alpha\mathbf{f}_L + \mathbf{f}_D \\ & \mathbf{M}\widetilde{\boldsymbol{\sigma}} - \mathbf{z}_1 = \mathbf{c}_1, \; \mathbf{z}_1 \le 0 \\ & \mathbf{N}\mathbf{x} - \mathbf{z}_0 = \mathbf{c}_0, \; \mathbf{z}_0 \le 0 \end{aligned} \tag{8}$$

Eventually, we can state the Upper Bound limit analysis formulation for this element as a standard Linear Programming (LP) (Eq. (7)), with the constraints of compatibility and flow rule for interfaces (Eq. (3b)) and elements (Eq. (6)), as well as a positive work condition for the external load [55]. In the objective function, we take into account all the dissipations induced by gravity, interface discontinuities, and element deformation. Observing the duality of the optimization problem (7) brings us to the static form of the UB formulation in terms of virtual power (Eq. (8)), providing information on the interfacial resultants and element stresses. In this optimization problem, we maximize the load multiplier of the system, subject to the constraint of the equilibrium and two constitutive constraints regarding interfaces and elements. The automatic remeshing can be further developed based on iteratively solving these two formulations, implemented as so-called sequential linear programming.

Despite enabling the velocity jumps, the overlapped nodes use the same index recorded in the database, given the merit of storage reduction and quick adjacency searching. This could further benefit the implementation of the remeshing, speeding up the procedure. When computing the matrices, we introduce another system of indices for nodal, interfacial, and element unknowns, where the velocities of the overlapped nodes are labeled separately. A reciprocal mapping of these two index systems has been built for a quick query, when necessary.

2.2. Establishment of automatic remeshing procedure

We now proceed to establish the automatic remeshing procedure to reduce the mesh dependence of the limit analysis results. The criterion of the refinement selection is based on the dissipation energy of the element deformation (index γ_i defined in Eq. (9a)). The element dissipation can be computed through the inner dot of the element cohesion vector $\mathbf{c}_{1,i}$ (defined in Eq. (5b)) and the corresponding plastic multiplier vector $\boldsymbol{\lambda}_i$ provided by the upper bound solution. In each iteration, we take priority to break the bulk with large deformation (set E_{re}^I), namely, the element whose index exceeds the predefined threshold $\alpha_e\gamma_{\max}$ (Fig. 3a). Here, we also penalize the element with a small area (see the

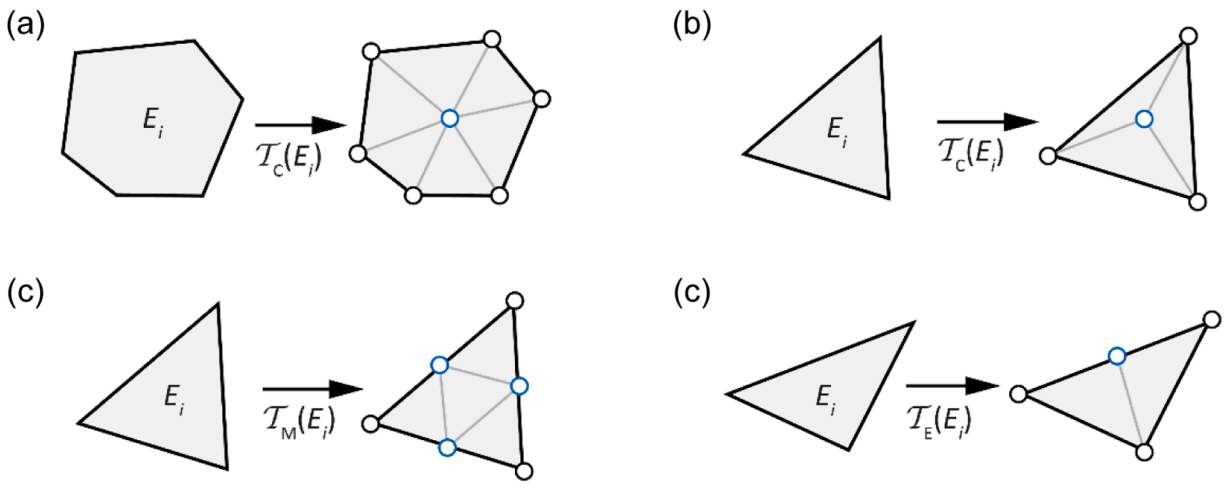

Fig. 4. Remeshing scheme for polygon and triangle elements at each iteration. (a) POLY: centroid refinement. (b) TRI: centroid refinement. (c) TRI: Mid-point refinement. (d) TRI: Edge-split method.

second term in Eq. (9a)) to avoid repeatedly refining the elements of the concentration-effect region. Another group of candidates for refinement comprises the elements that are contiguous to the interfaces with large dissipation (set E^J_{re} in Eq. (9b)). Similarly, we compute the dissipation for each interface according to the interfacial cohesion and multiplier vectors ($\mathbf{c}_{0,j}$ and $\mathbf{p}_j$) and select those with the dissipation exceeding the threshold $\alpha_c P_{\text{dj,max}}$. The elements associated with those joints will be included in the set for refinement, but with the exclusion of the elements that take those interfaces as edges (Fig. 3b, Eq. (9b)). Eventually, the elements that will be refined in this step (E_{re}) will be the union of the above two element sets (Eq. (9c)). Users are allowed to adjust two threshold parameters $\alpha_e < 1$ and $\alpha_c < 1$ to control the selection based on the interfacial or element dissipation, respectively. A smaller choice of α_e or α_c will certainly involve more elements being refined in one step while the large ones may give rise to a low convergence speed. The assignment of these two thresholds could be quite critical in practice.

$$E^I_{\text{re}} := \left\{ i | \gamma_i > \alpha_e \max_{i \in E} \{\gamma_i\} \right\}, \gamma_i := \underbrace{\frac{P^i_{\text{de}}}{\sum_{i=1}^{N_e} P^i_{\text{de}}}}_{\text{dissipation}} \cdot \underbrace{\frac{|E_i|}{\sum_{i=1}^{N_e} |E_i|}}_{\text{area penalty}}, P^i_{\text{de}} = \mathbf{c}^T_{1,i} \boldsymbol{\lambda}_i \tag{9a}$$

$$J_{\text{re}} := \left\{ i | P^i_{\text{dj}} > \alpha_c \max_{i \in J} \left\{ P^i_{\text{dj}} := \mathbf{c}^T_{0,j} \mathbf{p}_j \right\} \right\}, E^J_{\text{re}} := \{ i | E_i \text{ associated with joint } j \in J_{\text{re}} \} \tag{9b}$$

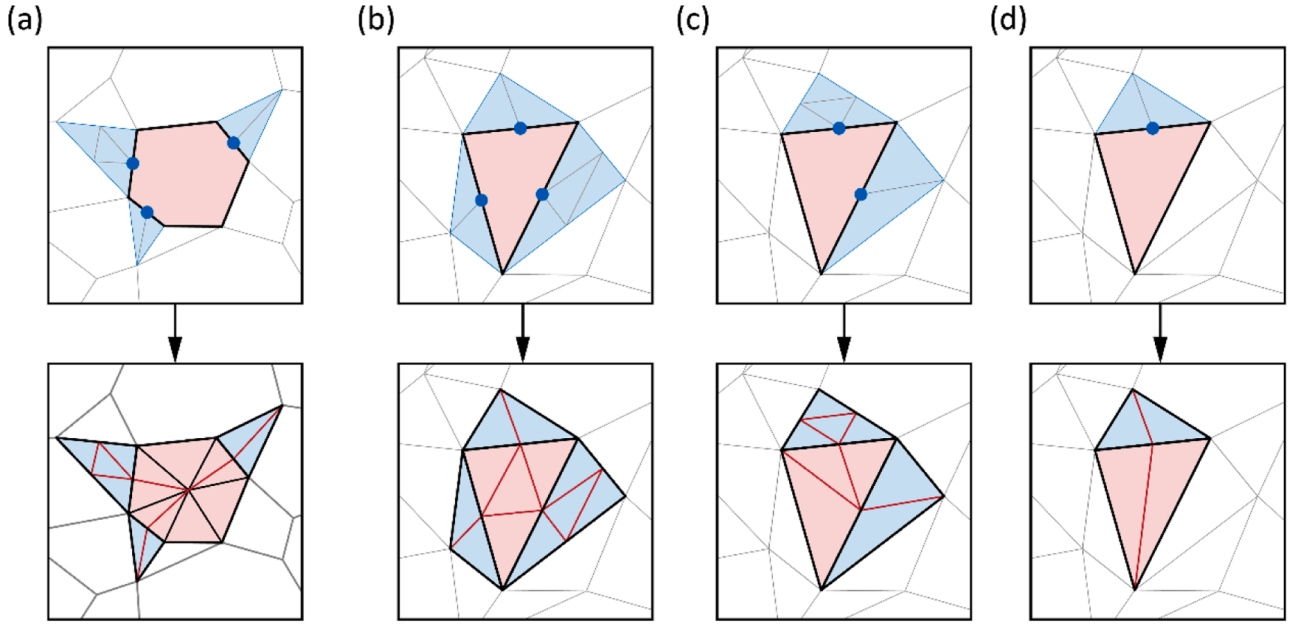

Fig. 5. Resolving the non-conformity in the mesh after the implementation of the element refinement scheme.

Algorithm 1
Iterative remeshing scheme.

1. Get the initial solution by solving Eqs. (7) and (8);
Initial sol.$\rightarrow\left\{\mathbf{u}_{\mathscr{P}}^{[0]},\tilde{\boldsymbol{\sigma}}^{[0]},\mathbf{x}^{[0]},\mathbf{z}_0^{[0]},\mathbf{z}_1^{[0]},\mathbf{p}^{[0]},\boldsymbol{\lambda}^{[0]},\alpha^{[0]}\right\}$
2. Initial setting: $e=1$, tol=0.001, $k=0$;
3. **WHILE** $e > tol$
4. $k=k+1$;
5. Define the element set for refinement E_{re} through Eqs. (9a)–(9c).
6. Refine element set E_{re} through refinement scheme $T_C/T_M/T_E$ (Fig. 4).
7. Resolve the non-conformity in the new mesh (Fig. 5)
8. Solve the new model through Eqs. (7) and (8) and get a new solution $\mathbf{u}_{\mathscr{P}}^{[k]}, \mathbf{p}^{[k]}, \boldsymbol{\lambda}^{[k]}, \alpha^{[k]}$
New sol.$\rightarrow\left\{\mathbf{u}_{\mathscr{P}}^{[k]},\tilde{\boldsymbol{\sigma}}^{[k]},\mathbf{x}^{[k]},\mathbf{z}_0^{[k]},\mathbf{z}_1^{[k]},\mathbf{p}^{[k]},\boldsymbol{\lambda}^{[k]},\alpha^{[k]}\right\}$
9. Calculate error $e=|\alpha^{[k]}-\alpha^{[k-1]}|/\alpha^{[k-1]}$
10. **END**

$$E_{\text{re}}=E_{\text{re}}^{I}\cup E_{\text{re}}^{J} \tag{9c}$$

After clarifying the selection of the element in each step, we propose specific refinement schemes for the elements. Selected non-triangular elements will be split into triangles (Fig. 4a), with an additional node assigned at the centroid. Regarding the triangular case, we propose three different schemes. The first approach is the direct application of the centroid refinement scheme previously for the polygons (Fig. 4b), bringing about the same subdivision to the adoption of [31]. The rest two are inspired by the proposal from Christiansen and Pedersen [28] for the structured mesh. The mid-point approach, the most popular scheme adopted in recent contributions (see for instance [37,38]), is a uniform and symmetric refinement (Fig. 4b). We add a node at the midpoint of each edge of the triangle, generating four similar sub-elements. As a result, the direction of the new interfaces always remains parallel to the original edge after such refinement. The edge-split refinement is simpler and more direct (Fig. 4c), where the element is split at the middle of the longest edge. The generation of the new elements is the fewest among all the three approaches. Several applications of such refinement have been recently presented (see [29, 30,32]).

Simply implementing the refinement scheme, the adjusted mesh will contain hanging nodes. Although such mesh non-conformity is allowed since interfacial velocity jumps have been taken into account in the limit analysis formulation, adopting a conforming mesh is usually more robust given the better continuity of slip-lines. For that purpose, after refining the target element, we immediately adjust the bulks around this element to keep the mesh conform. Below we give the scheme to resolve these hanging nodes (Fig. 5). For the polygon with non-conforming nodes, the centroid refinement is first implemented, followed by applying the edge split to the triangular patches with non-conformity (Fig. 5a). We directly implement the mid-point refinement to the triangles with hanging nodes on all three edges (Fig. 5b), and the rest cases can be resolved by sequentially applying the edge split method along the non-conforming edges once or twice (Fig. 5c and 5d).

Gathering all the previous steps, the whole iterative remeshing scheme can be stated as Algorithm 1. Implementing this loop, we continuously refine the discretization until the ultimate capacity of the structure finally converges to a stable value. Implementing this procedure, we will first conduct a series of comparative studies through the strip footing problem, for a better understanding of its performance. Then, the approach will be applied to analyze the collapse of a 2D masonry arch bridge with full consideration of backfill to test its robustness in a more practical scenario.

3. Comparative study on different procedure configurations

In this section, we investigate the collapse of weightless cohesive-

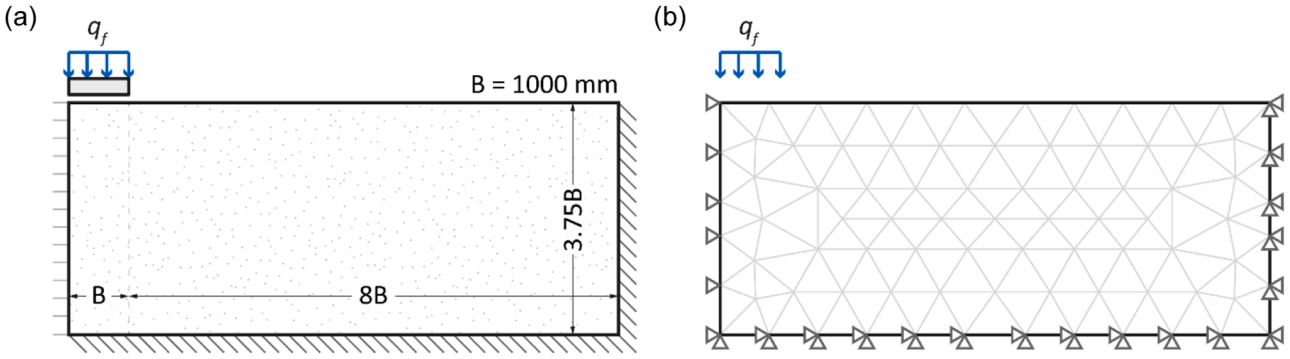

Fig. 6. Weightless cohesive-frictional strip footing benchmark. (a) Geometric features, load and boundary conditions. (b) Initial unstructured triangular mesh.

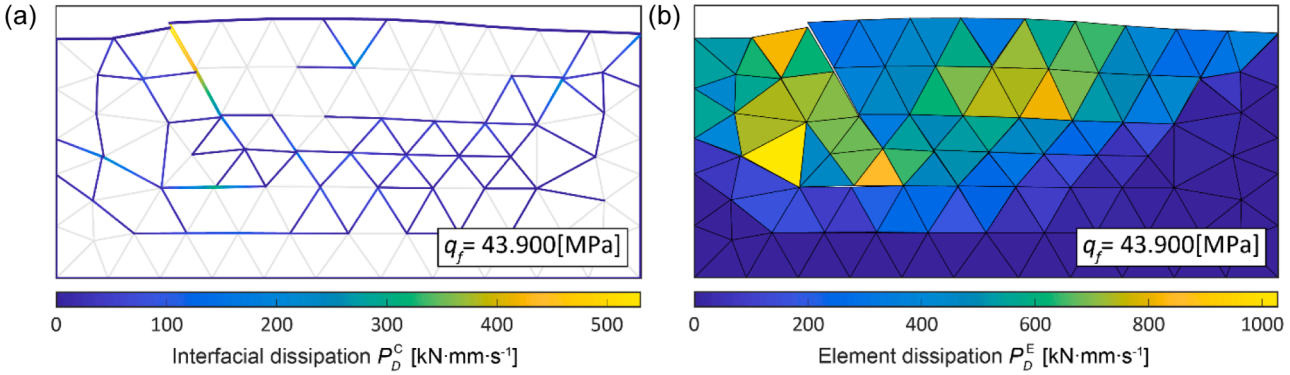

Fig. 7. Initial solution within the application of remeshing for the weightless cohesive-frictional strip footing problem, unstructured triangles, $p=24$. (a) Interfacial dissipation. (b) Element dissipation.

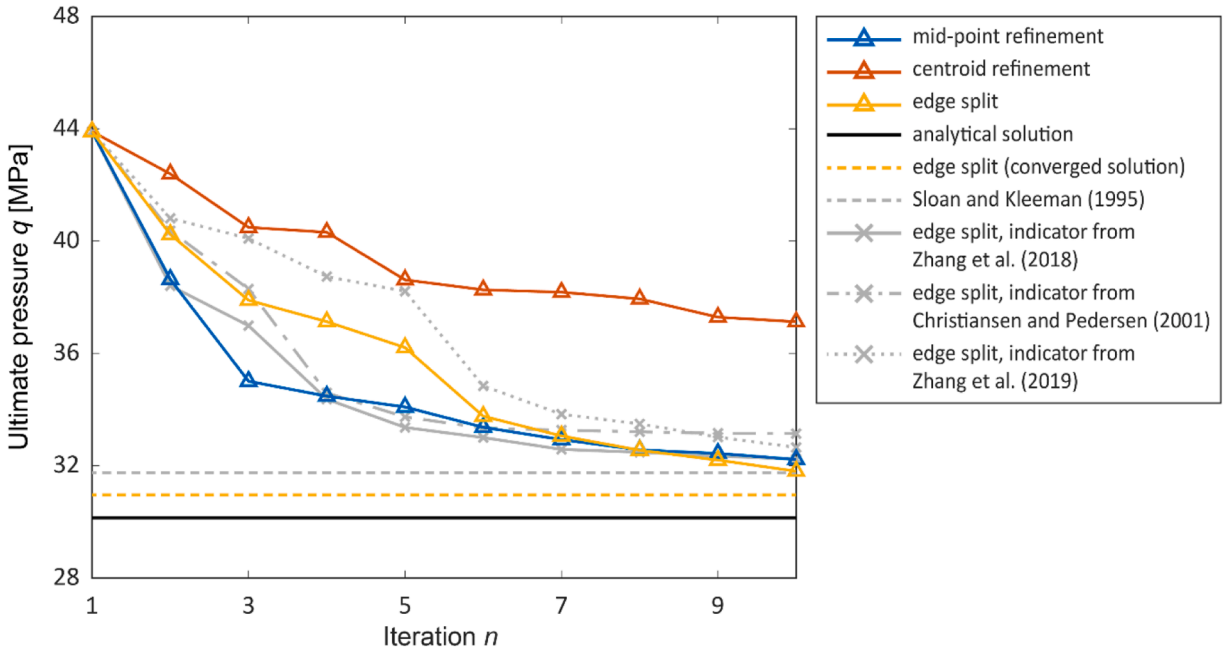

Fig. 8. Comparison among different triangular refinements during the remeshing procedure for the strip footing problem: convergence of ultimate pressure.

Table 1
Summary of the results and computational cost for the three refinement schemes, weightless cohesive-frictional strip footing problem with the application of automatic remeshing.

Remesh scheme	Indicator	$q_{f,[1]}$ [MPa]	$q_{f,[10]}$ [MPa]	Drop of load (%)	[a] Item count	[b]DOF	Time cost t (s)	[c]q [MPa]
Centroid refinement	Eq. (9c)	43.9	37.126	15.431	12,129	174,824	46.970	30.14
Mid-point refinement	Eq. (9c)		32.222	26.601	13,516	195,218	231.072	
Edge-split method	Eq. (9c)		31.807	27.547	3553	51,548	12.621	
	[30]		32.236	26.570	2597	37,220	8.327	
	[32]		32.651	25.624	1989	28,496	5.391	
	[28]		33.144	24.502	2031	28,820	6.106	

[a] The item here indicates the elements and interfaces used in the analysis.
[b] DOF represents the degrees of freedom used in the analysis.
[c] q denotes the analytical solution of weightless cohesive-frictional strip footing [3].

frictional strip footing, a simple but solid benchmark with analytical and numerical investigations [3], to test the effectiveness of this approach. We start from the unstructured triangular mesh to compare the performance of three refinement schemes proposed for triangles (see Fig. 4), and the best-performed scheme will be concluded. Secondly, we will test the robustness of the procedure when using polygon elements, where the necessity of resolving mesh non-conformity (Fig. 5) or filtering the small element (Eq. (9a)) will be additionally investigated.

3.1. *Different element refinements: unstructured triangular mesh*

Fig. 6 illustrates the geometry and boundary conditions of the strip footing subjected to a unit-width-surface ($B = 1000$ mm) pressure. The friction angle φ is 30° and the effective cohesion c is 1 MPa, taken in agreement with Sloan and Kleeman [3] for comparing purposes, despite that such cohesion could be quite high for a common geotechnical material. In any case, the results can be linearly scaled down to smaller cohesion cases if needed, given the system linearity. The constitutive model for the element deformation adopted is Mohr-Coulomb with no tension cutoff (Fig. 2a) and we keep the linearizing precisions equal to 24, as suggested in [3]. We start from the same initial solution (Fig. 7) predicted from a coarse unstructured triangular mesh (generated by "MESH2D" [56]), followed by the implementation of the remeshing procedure with different element refinements (see Fig. 4). The threshold factor for the selection criterion α_e/α_c is 0.4/0.6. Given the comparative purpose of this benchmark study, for each case, the procedure will stop at the 10th iteration whether the convergence criterion is reached or not, to control the computational budget at an acceptable level.

Fig. 8 gives the convergence curves of these 10 iterations for different refinement schemes, and the corresponding final predictions are collected in Table 1. The curve results have demonstrated the effectiveness of the proposed procedure. The system capacity prediction decreases by 15–28 % after those 10 iterations. However, the convergence speed and efficiency of employing different element refinements are discrepant. The performance of the centroid refinement is lower than our expectation. The final converged pressure is 23.2 % overestimated from the analytical solution. Such noticeable overestimation could stem from the fact that this refinement cannot help generate continuous cracking paths during the iteration. In the final iteration, we can note that numerous cracks propagate radially from the nodes but are not connected to configure a contiguous path (Fig. 10a and 10b). Nonetheless, it should be remarked that the characteristics of the discontinuity pattern generated by this scheme are naturally different from the continuous spiral slip-line assumed in the theoretical solution of the strip footing [57], resulting in a limited improvement of the collapse load prediction. The profit of this scheme could be different when applied to other collapse cases featuring radial or concentrated slip-lines.

In contrast, the mid-point refinement can give birth to better

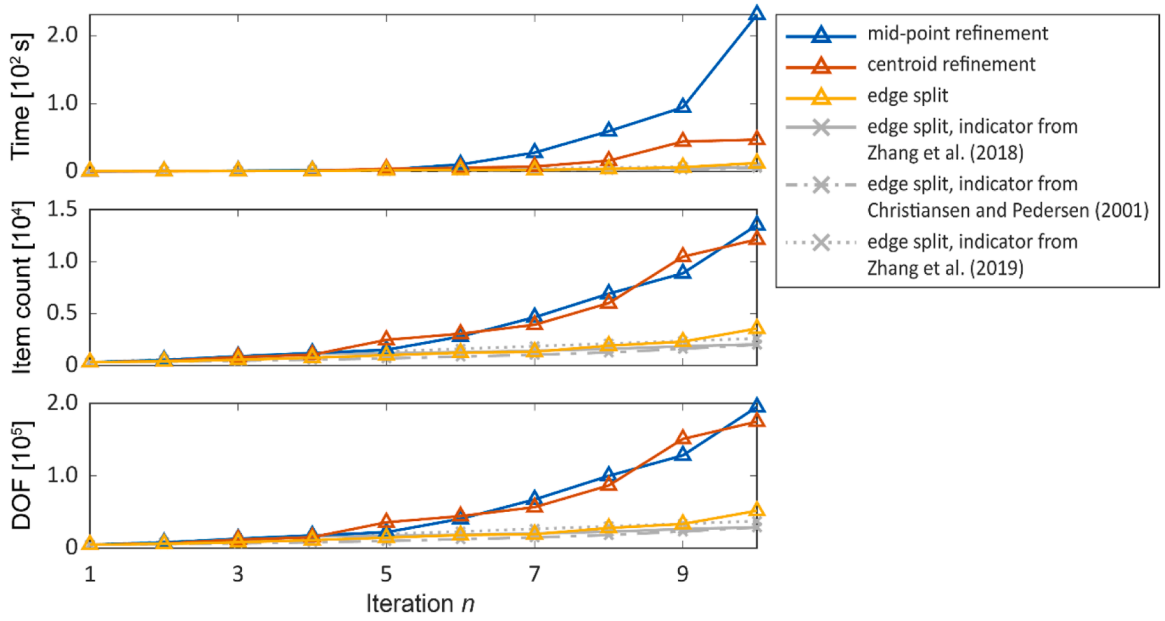

Fig. 9. Growth of the time cost, item count (elements plus interfaces), and degrees of freedom (DOF) during the remeshing procedure for the strip footing problem: comparison of different triangular refinements.

connective interface configurations since all the new joints are parallel to the original edges. The continuity of the initial mesh is well inherited during the iterations (Fig. 10c and 10d). The accuracy of the final prediction is thus very acceptable (about 6.9 % over the analytical solution). However, we would remark that some elements near the surface pressure are repeatedly split into tiny sizes, giving rise to an explosion of the item amount and analysis time in the late several iterations. In the last iteration, the time cost for the mid-point refinement can reach four times that of the centroid refinement (see Fig. 9 and Table 1).

The edge-split method presents the lowest time cost (6–27 % of the rest two approaches), as the newly generated elements are the fewest. The growth of the total number of elements/interfaces and degrees of freedom used in the analysis is also flatter than in the other two cases (see Fig. 9). The direction of the interfaces generated by this refinement is much more diverse, thanks to its unsymmetric feature. The connectivity of the interfaces typically remains after several iterations though (Fig. 10e and 10f). As a result, such refinement improves the diversity of the underlying slip-lines that the mesh can capture, bringing about very conservative load prediction. The given load prediction is the lowest among all the three considered approaches, with a deviation of only 5.5 % against the analytical solution. We also plot the converged solution given by the edge-split method (after 16 iterations), whose precision is further improved (2.5 % deviation). Such precision also exceeds the prediction from the finest structured triangular mesh reported in [3]. In summary, according to this benchmark study, the edge-split method is the best refinement scheme for the remeshing procedure. In the below application to the polygon mesh, we will employ only the edge-split method to refine triangular elements.

Figs. 8 and 9 also compare the usage of different element selection indicators. Reviewing the relevant literature, we select two indicators based on the dissipation [30,32] and one based on the plastic strain [28] to be compared with the indicator proposed in the present paper (Eqs. (9a)–(9c)), implementing the same edge-split refinement. The results indicate that typically, the selection of different indicators does not influence much the final predictions. Nonetheless, the utilization of dissipation-based indicators is more recommended, since the strain-based selection gives a slightly higher collapse load against all the others. The indicator proposed performs in the best manner with respect to the precision of the converged solution, an advantage which could be attributed to the inclusion of the area filter. Small elements are filtered out when constructing the refining set to avoid repeated subdivisions. Such a feature could be beneficial in some problems with concentration effects, avoiding the iterative searching being trapped at a local optimal point. Later in the text, this aspect will be further compared and discussed in detail applying the polygon discretization.

Nonetheless, we would finally note that the mechanism predicted in the edge-split case does not fully fit the actual solution, despite the accurate load prediction. The spiral boundary of the mobilized soil is not perfectly reproduced [57], for which the employment of the triangular elements could be blamed. Although the edge-split scheme proposed could bring in more slip angle variation, the discontinuity direction in a triangular mesh cannot be very diverse. Eventually, the generated interfaces after the remeshing are typically parallel or perpendicular to the edges of the initial mesh, and the potential slip direction is still too limited to represent a spiral boundary. We can only get a polyline slip boundary zig-zagging around the real spiral path. The results of the structured triangular meshes originally adopted by Sloan and Kleeman (see [3,44]) also produced a similar polyline slip boundary, basically in line with the triangular predictions presented in this paper. In contrast, we will soon illustrate below that using the polygon mesh can improve such deviated mechanism prediction. The centroid division of a polygon bulk naturally boosts the underlying slip directions in the system. A smooth polyline slipping path is apt to be generated and the theoretical spiral slip boundary can thus be perfectly reproduced.

3.2. *Application to polygon mesh: mesh non-conformity or area filter*

We proceed to investigate the performance of the remeshing procedure when incorporating polygon meshes. Two polygon discretizations with different shape regularities are taken into account, named random Voronoi and centroid Voronoi mesh, respectively, which are generated by the open-source package “lloydsAlgorithm” [58]. The threshold factor for the element selection criterion α_e/α_c is kept as 0.4/0.6. In this analysis, we set the convergence tolerance as 10^{-2} and the procedure will quit only when the error of collapse load decreases below this tolerance. As mentioned above, we apply the edge-split method for the triangular element and the centroid refinement for the polygons. Initial solutions for the two polygon meshes are given below (Fig. 11). These initial solutions are highly overestimated compared to both triangle predictions and the analytical solution, which is a

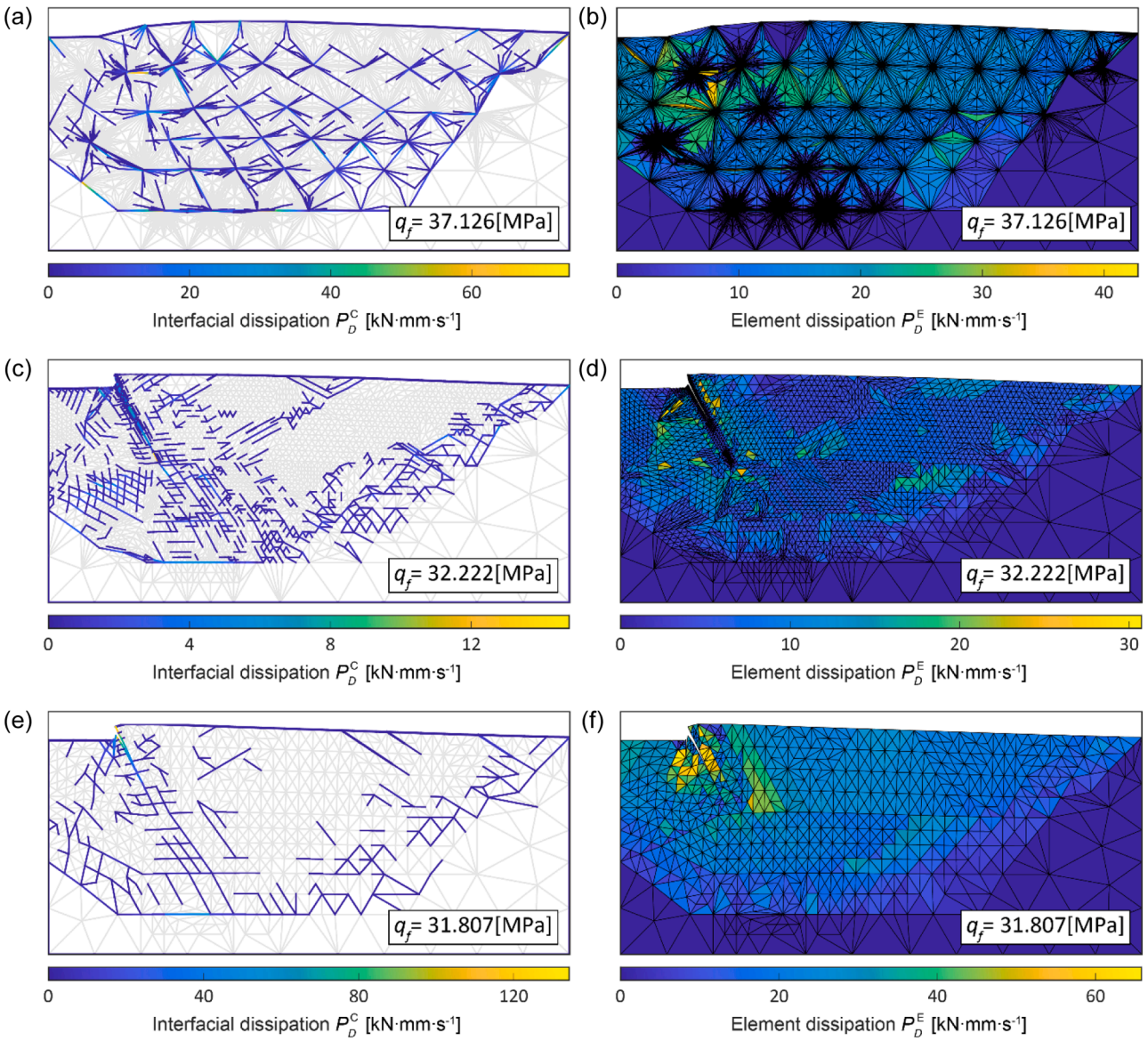

Fig. 10. Collapse mechanism for the strip footing problem with the application of remeshing. Comparison of different refinement schemes for triangular elements, final predictions. (a) Interfacial dissipation, centroid refinement. (b) Element dissipation, centroid refinement. (c) Interfacial dissipation, mid-point refinement. (d) Element dissipation, mid-point refinement. (e) Interfacial dissipation, edge split approach. (f) Element dissipation, edge split approach.

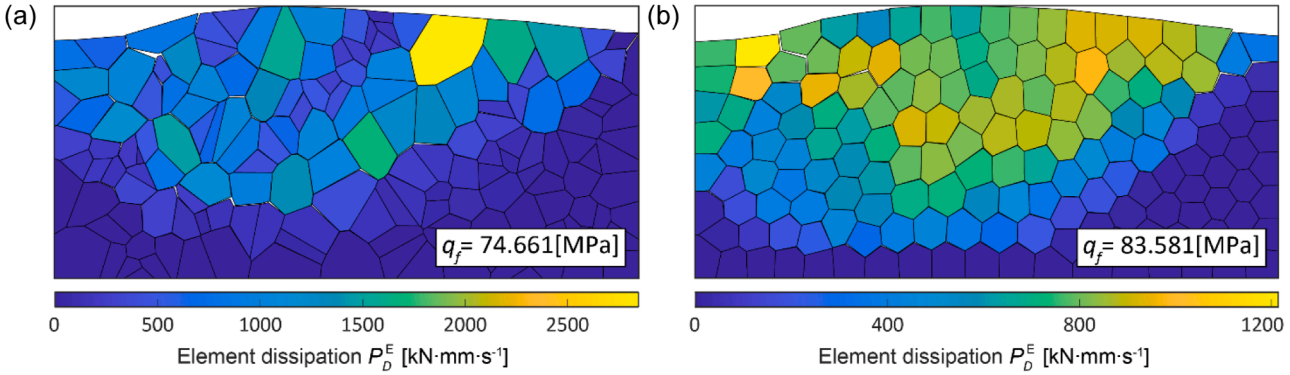

Fig. 11. Initial solutions of weightless cohesive-frictional strip footing for the application of remeshing procedure, polygon meshes, $p = 24$. (a) Random Voronoi mesh. (b) Centroid Voronoi mesh.

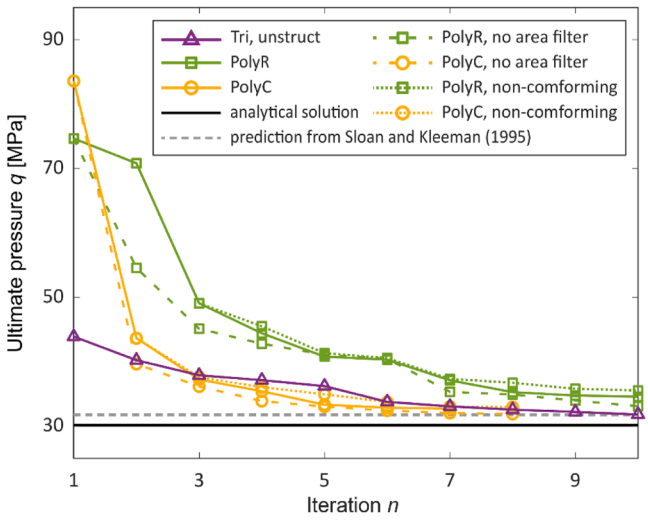

Fig. 12. Convergence of the collapse load during the remeshing procedure, weightless cohesive-frictional strip footing problem, comparison among different procedures.

demonstration of interior element locking arising from the constant-strain assumption (also reported in [44]). When the number of the element nodes increases, the description of its kinematic mode through the constant-strain field is no longer sufficient.

The proposed remeshing procedure can significantly reduce such a locking effect since the large-dissipation polygon bulks are successively split into locking-free triangular elements during the iteration. In both random and centroid Voronoi cases, the drop in the collapse load prediction is remarkable (about 53–60 % of the initial, see iteration curve in Fig. 12 and result summary in Table 2). Moreover, we can appreciate a curved boundary of the mobilizing soil in the final predicted mechanisms (see Fig. 14a and 14b), being very analogous to the spiral one assumed in the analytical solution [57]. In contrast, the primary crack patterns predicted in the triangle cases are all long and straight (see Fig. 10). This demonstrates that employing polygon discretizations can take into account more underlying collapse mechanisms and slip-line patterns, owing to the great diversity of the interface directions generated by the refinement.

The final collapse load from the centroid Voronoi mesh can get very comparable precision to the triangle case (about 3 %, see Fig. 12), with rather fewer iterations, element/interface count, and degrees of freedom required (Fig. 13). The deviation to the analytical solution is also acceptable (within 9 %). This may demonstrate the competitive efficiency of employing polygon elements against the traditional triangles in the remeshing procedure. Random Voronoi mesh gives a higher converged load (bias of 5.7 %) with also more iterations, indicating a lower efficiency of using irregular elements. The better performance of the centroid mesh could be attributed to its uniformity of element size. We can expect a homogeneous decrease of element dimension during the procedure and the angle among the new interfaces is also quite average (Fig. 14c and 14d). Oppositely, in the random polygon mesh,

Table 2
Results of the remeshing iterations for weightless cohesive-frictional strip footing with different procedure configurations, $p = 24$.

Element shape	α_e	α_c	Selecting criterion	Resolve non-conformity	$q_{f,[1]}$ (MPa)	$q_{f,\ [end]}$ (MPa)	Drop of load (%)	error (%)
Triangular mesh	0.4	0.6	With area filter	Yes	43.90	31.85	27.45	5.67
Random Voronoi	0.4	0.6	With area filter	Yes	74.66	34.57	53.70	14.70
			No area filter	Yes		32.82	56.04	8.89
			With area filter	No		35.54	52.40	17.92
Centroid Voronoi	0.4	0.6	With area filter	Yes	83.58	32.71	60.86	8.53
			No area filter	Yes		31.88	61.86	5.77
			With area filter	No		32.95	60.58	9.32

[a]The error of the predictions given here is compared to the analytical solution in [3]. For the weightless cohesive-frictional strip footing, the accurate ultimate pressure is 30.14 MPa.

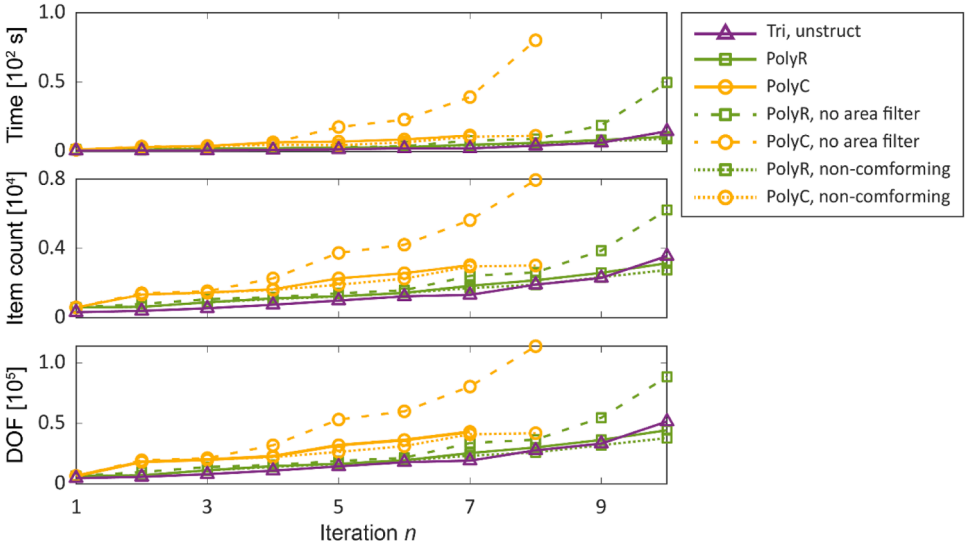

Fig. 13. Growth of the time cost, item count (elements plus interfaces), and degrees of freedom (DOF) during the remeshing procedure, weightless cohesive-frictional strip footing problem, comparison among different procedures.

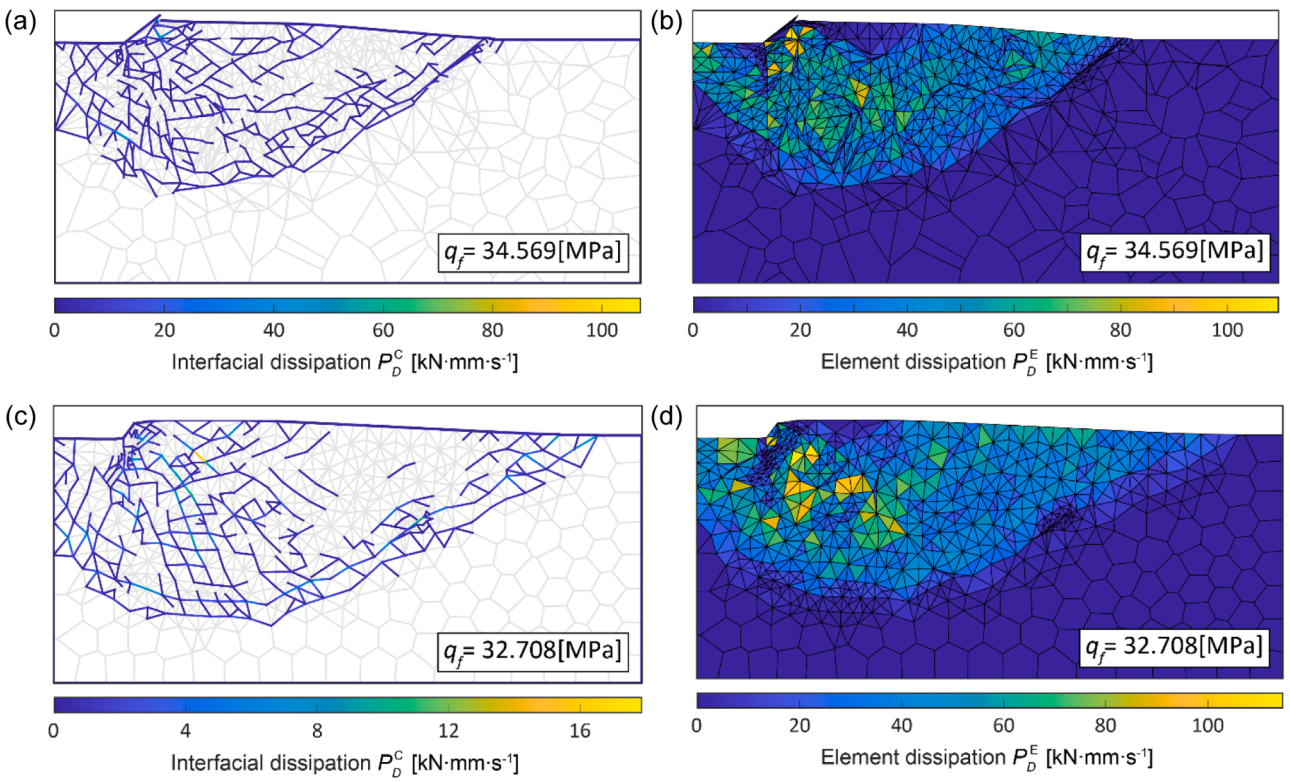

Fig. 14. Collapse mechanism for the strip footing problem with the application of remeshing in polygon meshes. (a) Random Voronoi mesh, interfacial dissipation. (b) Random Voronoi mesh, element dissipation. (c) Centroid Voronoi mesh, interfacial dissipation. (d) Centroid Voronoi mesh, element dissipation.

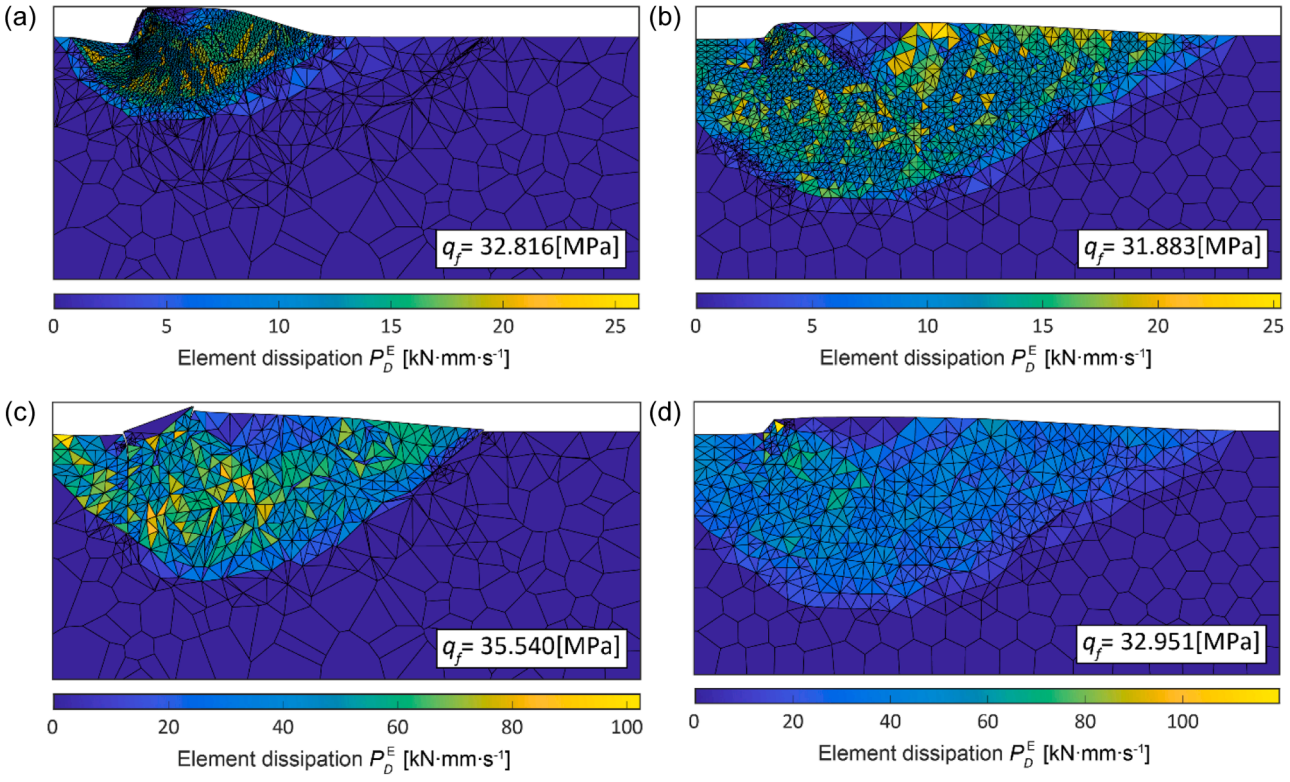

Fig. 15. Collapse mechanism for the strip footing problem with the application of remeshing in polygon meshes, comparison among different procedures, final predictions. (a) Random Voronoi mesh, without area filter. (b) Centroid Voronoi mesh, without area filter. (c) Random Voronoi mesh, non-conforming mesh. (d) Centroid Voronoi mesh, non-conforming mesh.

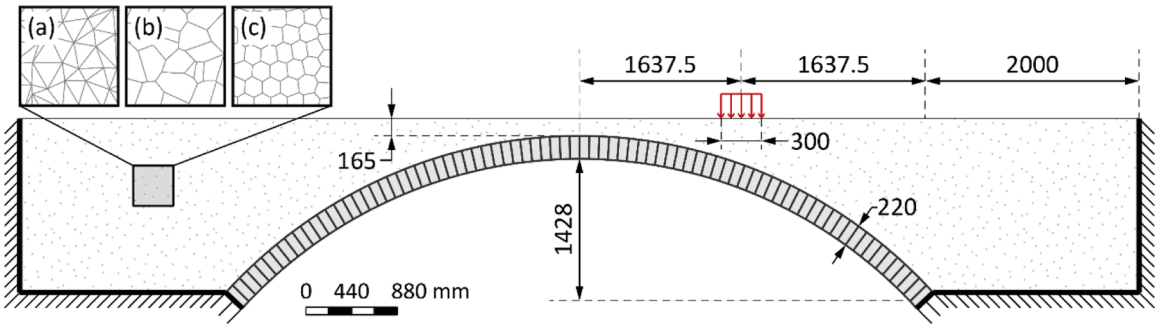

Fig. 16. Geometry features, mesh, load, and boundary conditions of Prestwood Bridge. (a) Unstructured triangles. (b) Random Voronoi. (c) Centroid Voronoi.

Table 3
Material parameters for the brick, backfill, and interfaces, Prestwood Bridge.

Elements			Interfaces		
brick	Density ρ_b [kg/m^3]	2000	Frictional angle	Brick to brick φ_{bb} [°]	37
	Compressive strength σ_{bc} [MPa]	4.5		Brick to backfill φ_{bf} [°]	37
	Tensile strength σ_{bt} [MPa]	0		Backfill to backfill φ_{ff} [°]	37
backfill	Density ρ_f [kg/m^3]	2000	Cohesion	Brick to brick c_{bb} [MPa]	10^{-6}
	Frictional angle φ_f [°]	37		Brick to backfill c_{bf} [MPa]	0.01
	Cohesion c_f [MPa]	0.01		Backfill to backfill c_{ff} [MPa]	0.01
	Tensile strength σ_{ft} [MPa]	0			

the procedure could repeatedly refine several tiny elements because of the large dispersion of the element size. We also notice the angle between some of the interfaces almost vanishes (Fig. 14a and 14b) in the last several steps, which makes the refinement less effective.

Recall that in the established remeshing procedure (Algorithm 1), we have involved a filter of the element dimension (second term of γ_i in Eq. (9a)) in the selecting process to avoid the over-refinement of some small elements, with the resolve of the non-conformity induced by the element refinement (see Fig. 5). At the end of this section, we also give the remeshing process of the two polygon meshes without the area filter and the settlement of mesh non-conformity, respectively, as a short demonstration of the necessity of including these aspects.

Involving the dimension filter is quite essential in particular for the mesh with poor regularity. After the removal of the filter, we can see that the element size of the random Voronoi mesh has been reduced to a very low level at the end, and the predicted mobilizing soil is remarkably shrunk (compare Fig. 15a to Fig. 14b). Such over-refinement is also inefficient. As the curve results indicated (Fig. 13), removing the dimension filter leads to 5–8 times boosting the time consumption but with a precision improvement of only 1–3 % (Fig. 12). The elements/interfaces and degrees of freedom required in the analysis also rise about 4 times (Fig. 13). Comparatively, the prediction from the centroid mesh is less affected by whether this filter is involved (Fig. 15b). We still remark on the explosion of the computational cost after deactivating this filter though (Fig. 13).

Without settling the non-conformity does not make a remarkable difference in the final prediction. The final mechanism prediction of both two polygon meshes considered (compare Fig. 15c and 15d) are in good consistency. Using non-conforming mesh might only lead to slightly higher load prediction and lower convergence speed (see centroid case in Fig. 12), but the discrepancy is quite limited (e.g. within 3 % regarding load prediction, see Table 2). Nonetheless, given the fair demand of this module for the computational budget, we will continue to settle the non-conformity of the mesh during the iterations.

4. Application study: collapse analysis of masonry arch bridge with fill

This section will apply the established approach to a more practical scenario: collapse analysis of a masonry arch bridge. Typically, fill material will be employed to cover the arch ring of the bridge up to the deck. However, this feature is commonly ignored or improperly considered in recent numerical simulations (e.g., [14]). Below we will employ the limit analysis to investigate this problem, featuring continuous modeling for the backfill part. The proposed remeshing procedure will be applied to the fill region.

We take Prestwood Bridge as a benchmark example since it has been on-site tested by previous researchers. The geometry, boundary, and load condition (Fig. 16), as well as the material features of the elements and interfaces (Table 3) are given below, according to the previous numerical works on this bridge [53,54]. The constitutive model for the backfill is Mohr-Coulomb criterion with tension cut-off (Fig. 2b). The vault of the bridge comprises a single ring of 80 bricks laid as header. The modeling of these bricks adopts the axial-deformable element proposed in [59], mimicking the bending behavior of beam elements. The constitutive for the brick deformation is No-Tension Material (NTM)

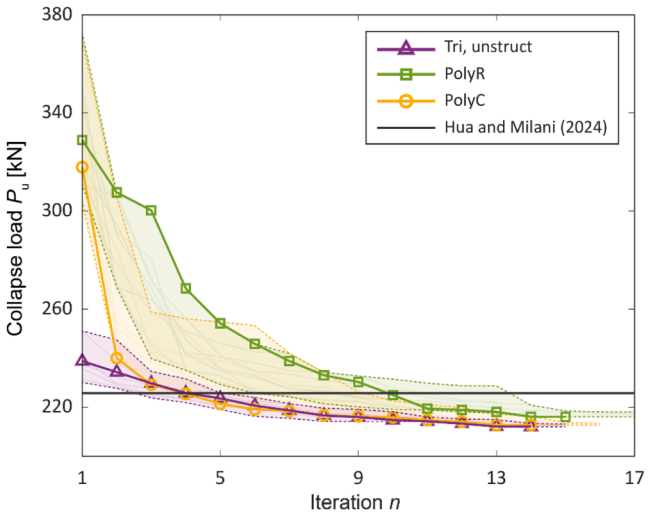

Fig. 17. Convergence of the collapse load during the remeshing procedure, Prestwood Bridge, axial deformable ring with quadrilateral linearization.

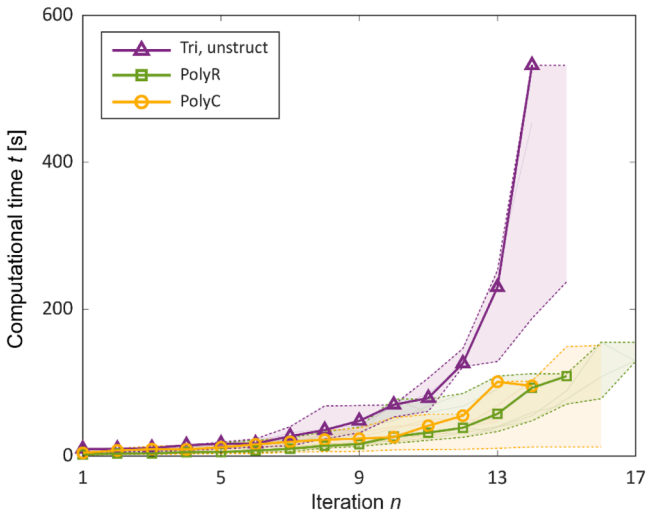

Fig. 18. Growth of the computational time during the remeshing procedure, Prestwood Bridge, axial deformable ring with quadrilateral linearization.

with quadrilateral linearization (see [59] for more details). Despite supplementing the features above, the limit analysis formulation of this problem can still be written as the consistent Linear Programming (LP) as Eqs. (7) and (8). To test the robustness of the remeshing procedure for different element shapes, we again account for the unstructured triangular, random Voronoi, and centroid Voronoi discretizations (Fig. 16), employing the same mesh generator [56,58].

4.1. Application of remeshing procedure

Regarding the automatic remeshing procedure, we use the configuration with the best robustness and efficiency concluded in the previous benchmark study, i.e. employing centroid refinement for the polygons and edge-split method for the triangles with element dimension filter and settlement of mesh non-conformity. The threshold setting for the refinement selection α_e/α_c is the same 0.4/0.6. The convergence tolerance reduces to 10^{-3}. To also investigate the effect of initial mesh, we test 8 different meshes for each element shape case, featuring different initial sizes and randomness.

Fig. 17 illustrates the envelope region of these 8 iteration curves for each shape case, highlighting the one with the lowest converged load prediction. In Fig. 18, we give the counterpart curve plots regarding the time consumption. Table 4 summarizes the average and coefficient of variation of the final load predictions with different initial mesh configurations. Comparing the initial solutions from triangular and polygon discretizations, we can note the same locking effect observed in the previous strip footing problem. The collapse load predicted from the two polygon meshes is 37 % higher than the triangle result. Such overestimation is moderated compared to that noticed in strip footing though, which should be attributed to the minor restriction of the boundary condition. The boundary of the two wings of the backfill is far away from the loading area. Note that all converged solutions provide a collapse load smaller than that obtained in [59] (Table 4), where the bridge was studied through a 2D upper bound limit analysis code not equipped with remeshing, indicating the effectiveness of the approach proposed.

The performance of the remeshing procedure is also very prominent when applied to this case study. The load decrease for all the meshes considered is significant during the refinement (about 11.7–33.8 %). The element refinement majorly takes place at two large dissipation regions of the backfill: the load dispersion zone at the right and the passive motion zone at the left. The collapse mechanism of the arches basically does not change during the iteration (see Figs. 19–21). Analogously, the remeshing procedure effectively resolves the locking of the constant-strain polygon element, where the load drop in the polygon mesh cases is significantly higher than the triangle one (34 % vs. 10 %, see Table 4 and Fig. 17). Eventually, the converged load predicted from the polygon and triangular meshes can get comparable precision.

On the other hand, we note a more rapid growth of the time cost in the triangular case. In the last several iterations, it can reach almost twice to five times that of using the polygon meshes (Fig. 18), despite fewer iteration steps required for the convergence. This implies the higher efficiency of using polygon elements in a large-scale application, probably owing to its shape complexity. Similar to what we have observed in the strip footing, the centroid division of the polygons can remarkably increase the diversity of the interface direction in the system. As a result, complex and irregular slip-line patterns can be simulated through fewer elements. Oppositely, the interfaces in the triangular mesh are almost parallel and the produced cracks pattern is straight and regular. Therefore, despite the numerous elements used, the external enveloping crack of the passive motion zone cannot evolve into a continuous path at the end of the iteration (see Fig. 19e and 19f), suppressing the passive mobilization of the backfill to some extent. In the centroid Voronoi case, we can appreciate a slightly narrow refinement zone at the left with fewer elements (Fig. 21e and 21f).

Employing the irregular bulk gives rise to a slightly higher load prediction (about 2 %) while the accuracy is still acceptable. However, the element regularity demonstrates more influence on the efficiency of the remeshing iterations. Better shape regularity brings about a higher converging speed at the early stage as well as slightly fewer iterations required. This should be owing to better size uniformity of the discretization. New triangular elements generated from the regular polygon will have uniform sizes with no severe distortion or excessive aspect ratio (compare Figs. 20 and 21), which makes the refinement more efficient. Element irregularity also introduces more randomness in the discretization. In the random Voronoi case, we can observe a larger envelope region during the iteration due to the initial mesh variation (Fig. 17), and the discreteness of the final converged load is also higher (Table 4). In addition, although the envelope area in the triangular case is the narrowest, the randomness of the final load prediction might be

Table 4
Discreteness of the load prediction due to the employment of different initial meshes.

Element shape	[a] $\mu(P_{u,[1]})$ (kN)	[b] $CV(P_{u,[1]})$ (%)	$\mu(P_{u,[end]})$ (kN)	$CV(P_{u,[end]})$ (%)	Drop of load (%)	Prediction from [59] (kN)
Triangular mesh	239.537	3.31	215.169	1.18	10.17	225.747
Random Voronoi	334.496	6.05	219.978	2.03	34.24	
Centroid Voronoi	329.925	6.52	216.256	1.00	34.45	

[a] $\mu(\cdot)$ represents the average of the variable.
[b] $CV(\cdot)$ denotes the coefficient of variation, defined as the standard deviation over the mean.

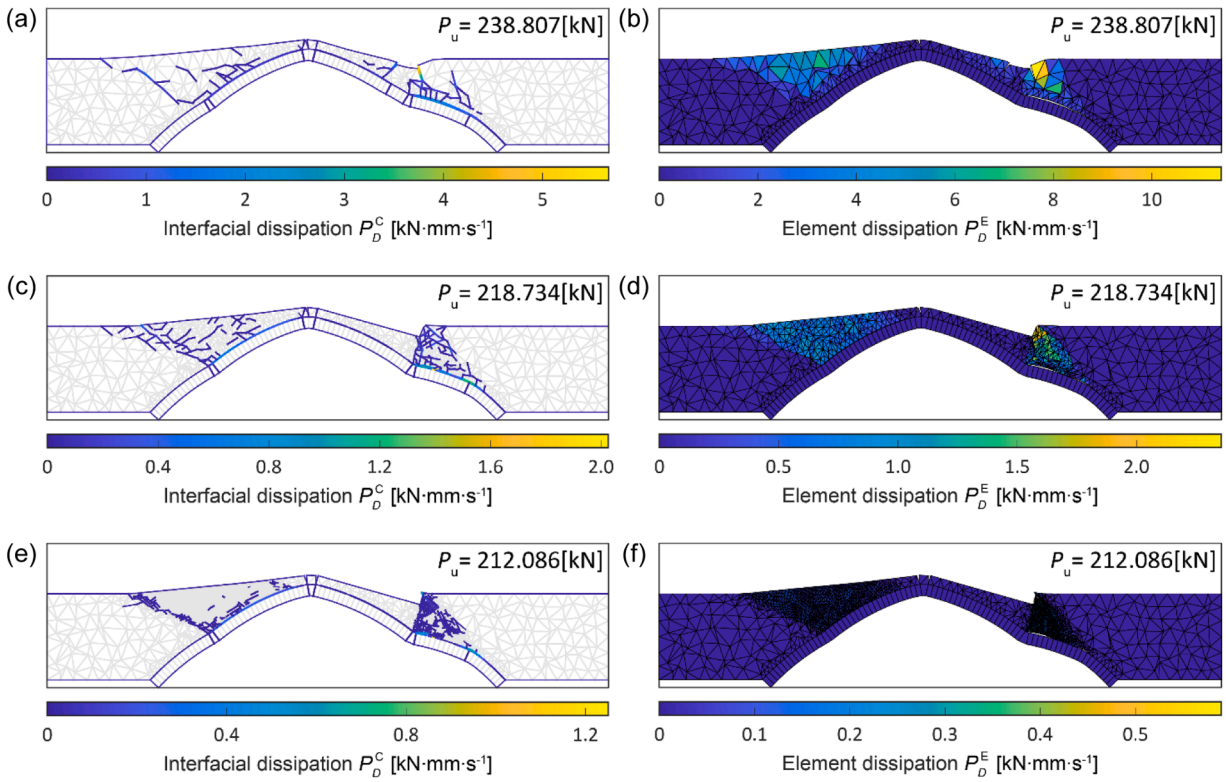

Fig. 19. Collapse mechanisms obtained for the Prestwood Bridge applying automatic remeshing, unstructured triangular mesh, and axial deformable ring modeling with quadrilateral linearization. (a) Initial solution, interfacial dissipation. (b) Initial solution, element dissipation. (c) Middle stage of the procedure, interfacial dissipation. (d) Middle stage of the procedure, element dissipation. (e) Converged prediction, interfacial dissipation. (f) Converged, element dissipation.

higher than the polygon one.

4.2. Comparison to the global mesh refinement

Finally, we implement traditional global refinement, compared to the proposed local remeshing approach. A sensitivity analysis on the size of the backfill element is conducted, where the size varies from 0.05 to 0.01 of the bridge span. Fig. 22 illustrates the curve of the load prediction as well as the corresponding computational time required. We collect all the critical results from the remeshing procedure and global refinement in Table 5 for comparison purposes. The required item count (elements plus interfaces) and degrees of freedom for each analysis are additionally provided.

It is obvious to appreciate from the summary of Table 5 the prominent efficiency of the remeshing procedure compared to the classic global refinement. Taking less than 1.5 % time consumption of the global refinement, the local remeshing approach can give rise to a more significant decrease in the load, with more conservative load predictions converging. The items and degrees of freedom required for the computation could decrease by 40 % after applying the remeshing technique. Moreover, the simple usage of the global approach cannot resolve the locking effect of the polygon elements. In the two polygon cases, a significant overestimation of the collapse load when compared with triangularization is always present even though a very refined mesh is employed. However, the counterpart predictions applying local remeshing have both converged to a more conservative level. The low efficiency of the global refinement should stem from the assignment of the fine mesh at the low dissipation region, which is completely unnecessary (compare Figs. 19 and 21 with Fig. 23). In general, we can conclude that the proposed remeshing procedure can speed up the analysis particularly in a large-scale scenario, instead of the classic global approach.

5. Discussion

Recall that the simple edge split method demonstrates exceptional performance against the other triangularization refinement in the comparative study of weightless cohesive-frictional strip footing. It can give very accurate converged load prediction (10 % deviation from the analytical solution) with the lowest time consumption. In contrast, as mentioned in the introduction, recent works have dominantly adopted the mid-point refinement approach when conducting the *h*-refinement (see [37,38]), which has been demonstrated to be not as efficient as expected according to our benchmark study. The computational cost of the mid-point refinement could be 4–5 times that of the edge split method, although their precisions can be comparable. Employing the mid-point refinement could be affordable providing that the discontinuities are not allowed in the formulation, which is the situation of the literature mentioned above. In that case, the refinement only increases the element unknowns, with no extra interface variables introduced. The corresponding growth of time consumption might still be acceptable. Once the formulation includes the interfacial velocity jumps, using such refinement will give rise to the explosion not only of the total number of the elements but also of that of the interfaces, resulting in very time-consuming analyses. Therefore, the mid-point refinement could no longer be a wise alternative for remeshing. Correspondingly, we notice that the edge split method is more popularly adopted in the literature that includes the interfacial velocity jumps in the limit analysis (see [29,30,32]).

Internal locking of constant-strain polygon elements could be a crucial drawback that halts its application [44], which could be effectively resolved through the proposed polygon-to-triangle refinement. The converged load predictions from the polygon meshes are comparable to the triangle one, in both cases considered. This could, on the other hand, demonstrate that actually, using the constant-strain polygon in some low-dissipation regions does not degrade too much accuracy.

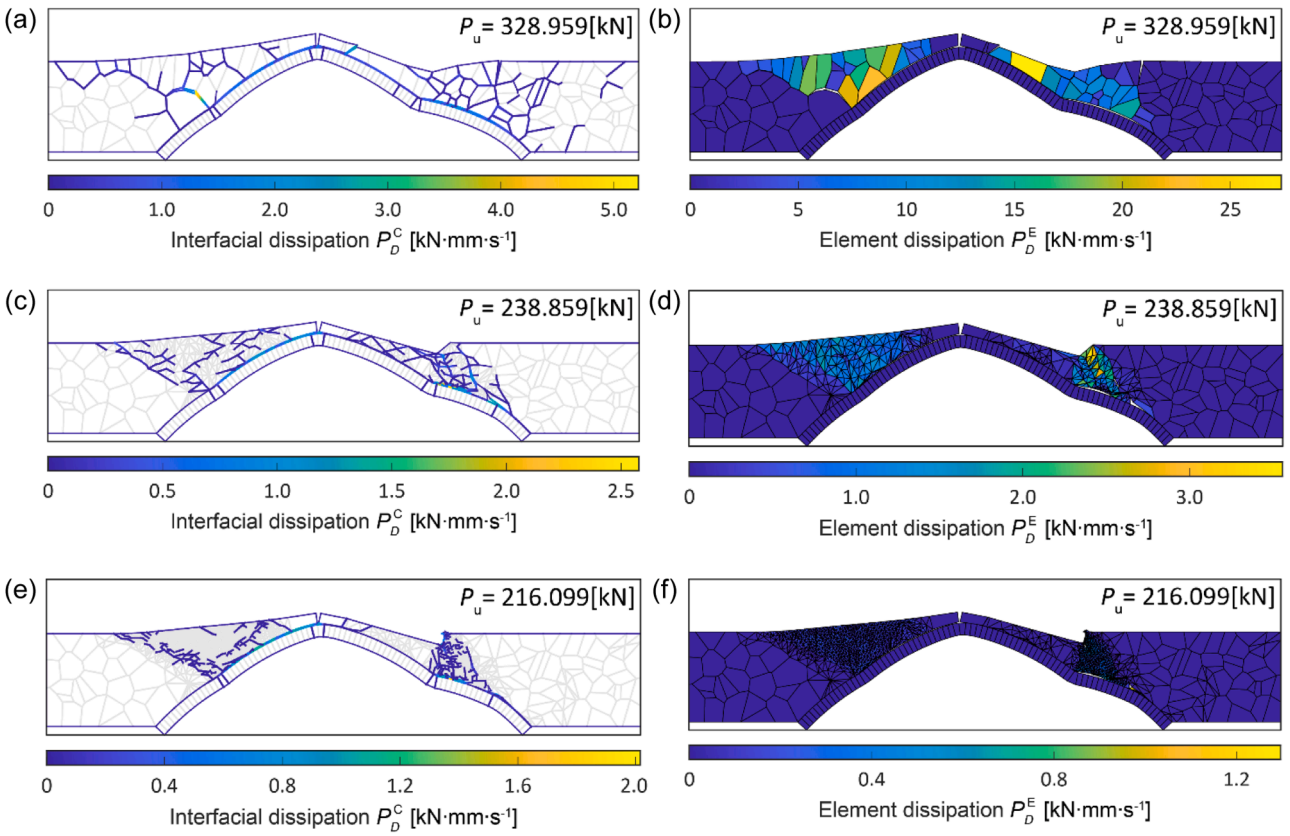

Fig. 20. Collapse mechanisms obtained for the Prestwood Bridge applying automatic remeshing, random Voronoi mesh, and axial deformable ring modeling with quadrilateral linearization. (a) Initial solution, interfacial dissipation. (b) Initial solution, element dissipation. (c) Middle stage of the procedure, interfacial dissipation. (d) Middle stage of the procedure, element dissipation. (e) Converged prediction, interfacial dissipation. (f) Converged, element dissipation.

However, in the polygon cases, the element amount assigned in those regions is significantly reduced against the triangular case, due to the fact that unnecessary triangulation is avoided. Instead, we can use a much finer mesh in the high-dissipation area to improve the precision. This could explain the competitive efficiency of using polygon elements in the remeshing procedure. Furthermore, remeshing of polygon discretizations can give rise to more diverse interface directions, differing from the parallel interfaces characterizing the triangular case. As we have discussed, such limited slip directions in the triangular mesh could lead to the deviation of the mechanism prediction (see Fig. 10). Polygon discretization has a great edge in this regard, a feature which could make it more robust in coping with some problems with complex slip-line patterns. The collapse mechanism with lower dissipation is more likely to be captured.

The limit analysis of Prestwood Bridge has been documented in many pioneering numerical contributions (see [53,54,59–61]) to understand the role of backfill, for which typically a uniform triangularization was adopted. It should be noted that our predictions, obtained with the remeshing technique, are always on the conservative side (see Table 4). The corresponding mechanisms are also accurate. Referring to a previous paper that uses exactly the same modeling strategies for the bridge [59], such improvement of the load prediction could reach 5 % (as illustrated in Fig. 17), demonstrating the profit of applying the remeshing procedure. Moreover, our predictions are also close to the previous experimental investigation [62], with a consistent collapse mechanism, although we highlight that the experimental collapse load should not be regarded as benchmark value, since experimental data cannot be considered a reference to validate numerical approaches characterized by the assumption of very specific mechanical and geometrical properties. The bridge has been standing for a long period with damages and existing cracks, and the corresponding material test for this bridge is not available. The material parameter adopted here refers to relevant numerical calibrations [53,54].

Future work will continuously investigate the robustness of this approach under more scenarios. As we have observed in the strip footing problem, the arrangement of the interfacial directions could be critical to the final collapse prediction due to including the interfacial discontinuities. The theoretical mobilization of the soil in the strip footing is impossible to represent by the interfacial pattern generated from the centroid refinement for the triangles, whose performance is thus limited. We will test more problems with different features of the slip-lines to comprehensively understand the performance of these three refinements. Additionally, we note that some contributions have developed adaptive techniques that can automatically adjust the direction of the interfaces [48,63], which could be absorbed in our future work to improve the robustness of this procedure.

6. Conclusions

This paper has explored suitable algorithms for remeshing in computational limit analysis with deformable elements, also allowing interfacial discontinuities. The approach is compatible not only with classic triangular elements but also with general arbitrary polygon discretizations. The iterative remeshing is based on the dissipation of the elements. Implementing this approach, the weightless cohesive-frictional strip footing problem has been first taken into account as a preliminary benchmark to understand the performance of different procedure configurations. Then, the collapse of a masonry arch bridge with full modeling of the backfill has been considered. The aforementioned case studies have demonstrated the effectiveness and robustness of the proposed remeshing procedure, even applicable to complex practical scenarios.

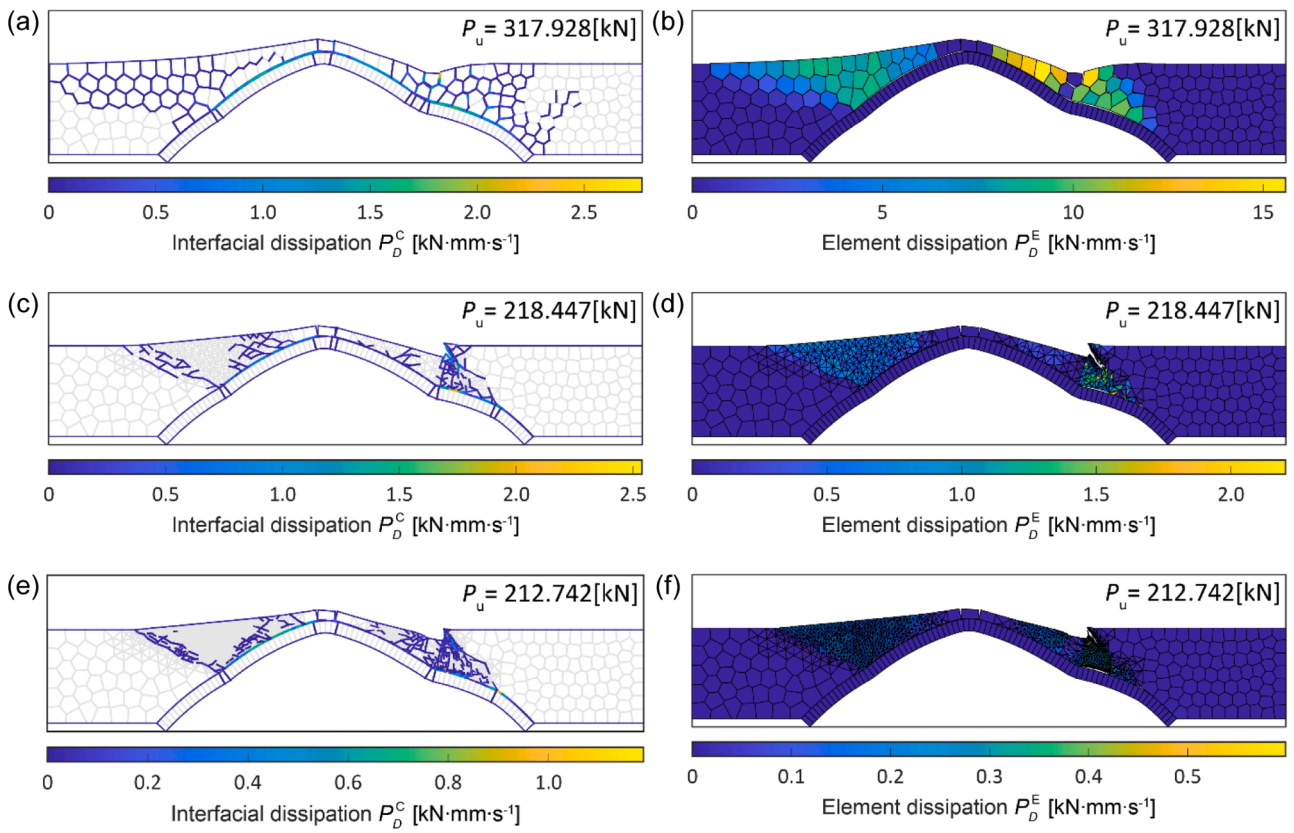

Fig. 21. Collapse mechanisms obtained for the Prestwood Bridge applying automatic remeshing, centroid Voronoi mesh, and axial deformable ring modeling with quadrilateral linearization. (a) Initial solution, interfacial dissipation. (b) Initial solution, element dissipation. (c) Middle stage of the procedure, interfacial dissipation. (d) Middle stage of the procedure, element dissipation. (e) Converged prediction, interfacial dissipation. (f) Converged, element dissipation.

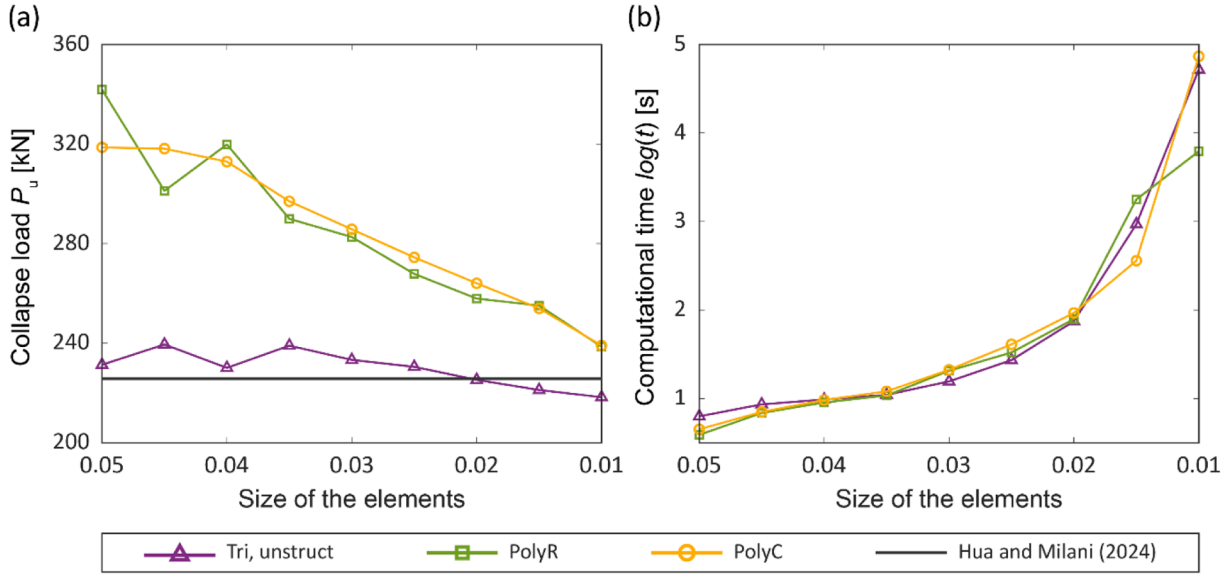

Fig. 22. Prestwood Bridge, results obtained with uniform mesh refinement, axial deformable ring with quadrilateral linearization. (a) Collapse load. (b) Computational time.

The comparative study on triangular refinements has demonstrated the best performance of the simple edge split method, as far as both precision and computational costs are concerned. The inclusion of an area filter in the element selection procedure has proved to be necessary for an efficiency increase. Applying polygon discretizations could bring about a more efficient analysis than traditional triangular meshing, on the condition of similar precision, particularly in large-scale scenarios. According to our investigation of the bridge collapse, the required time

Table 5
Comparison of the effect of remeshing procedure and global refinement, Prestwood Bridge.

	Element shape	[a]P_u (kN)	Drop of load (%)	[b]Item count	[b]DOF	[b]Time (s)
Automatic remeshing	Triangular mesh	215.169	10.17	6653	96,005	179.3
	Random Voronoi	219.978	34.24	5174	72,712	88.17
	Centroid Voronoi	216.256	34.45	4537	63,416	60.05
Global refinement	Triangular mesh	218.315	5.633	16,004	230,312	52,082
	Random Voronoi	238.612	30.20	18,622	197,312	6214
	Centroid Voronoi	239.055	24.98	18,611	197,268	73,562

[a] We choose the results of 0.01 element size as the final prediction for the global refinement case. Regarding automatic remeshing, the mean of the final prediction with different initial meshes is given.
[b] Regarding the remeshing cases, the mean values of these items in the converged prediction with different initial meshes are given. "Item count" in the table indicates the number of elements plus interfaces used in the analysis.

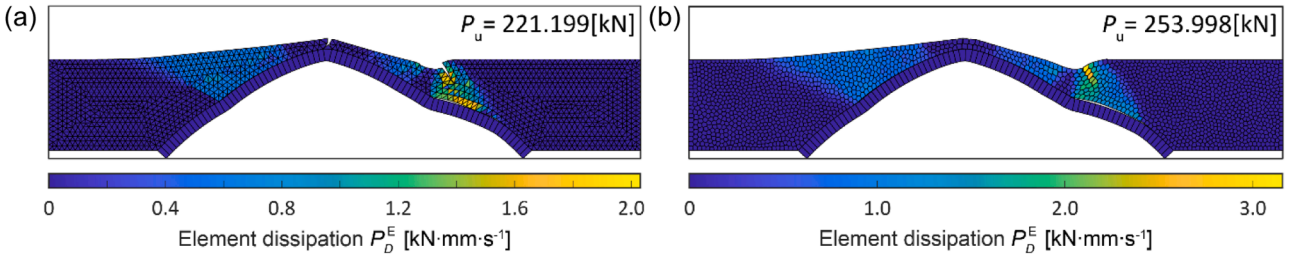

Fig. 23. Collapse mechanism for Prestwood Bridge obtained with a fine mesh (element size: 0.015 of span), application of uniform global refinement, axial deformable ring modeling with quadrilateral linearization. (a) Unstructured triangular mesh. (b) Centroid Voronoi polygon mesh.

cost of polygon meshes has been only 1/5–1/2 of the triangular counterpart. Polygon discretizations also perform more robustly in capturing complex slip-line patterns when predicting the collapse mechanism, given that the diverse potential slip directions can be generated from the element refinement. Those advances could imply the promising application of the polygon elements when incorporated with mesh adjustment techniques. In addition, the proposed remeshing can effectively reduce the inner locking of the polygon mesh induced by the constant-strain assumption.

CRediT authorship contribution statement

Yiwei Hua: Writing – review & editing, Writing – original draft, Visualization, Validation, Software, Methodology, Funding acquisition, Conceptualization. **Gabriele Milani:** Writing – review & editing, Supervision, Resources, Methodology, Funding acquisition, Conceptualization.

Declaration of competing interest

The authors declare that they have no known competing financial interests or personal relationships that could have appeared to influence the work reported in this paper.

Acknowledgments

Yiwei Hua would like to thank the financial support from China Scholarship Council (CSC) under the grant CSC No. 202108320019.

Gabriele Milani gratefully acknowledges the financial support of the Italian Ministry of Scientific Research MUR within the research project PRIN-2022 (https://www.dabc.polimi.it/en/progetto/advanced-mechanical-models-and-computational-methods-for-large-scale-3d-printing-of-innovative-concrete-structures/) titled "Advanced mechanical models and computational methods for large-scale 3D printing of innovative concrete structures (COMˆ3D-CREATE)" (National PI: Prof. Andrea Chiozzi, Local PI: Prof. Gabriele Milani). Finanziato dall'Unione europea- Next Generation EU, Missione 4 Componente 2 CUP D53D23004070006, M4C2 – Investimento 1.1 – Fondo per il Programma Nazionale della Ricerca (PNR) e Progetti di Ricerca di Rilevante Interesse Nazionale (PRIN).

Data availability

Data will be made available on request.

References

[1] Anderheggen E, Knöpfel H. Finite element limit analysis using linear programming. Int J Solids Struct 1972;8:1413–31. https://doi.org/10.1016/0020-7683(72)90088-1.
[2] Sloan SW. Upper bound limit analysis using finite elements and linear programming. Int J Numer Anal Methods Geomech 1989;13:263–82. https://doi.org/10.1002/nag.1610130304.
[3] Sloan SW, Kleeman PW. Upper bound limit analysis using discontinuous velocity fields. Comput Methods Appl Mech Eng 1995;127:293–314. https://doi.org/10.1016/0045-7825(95)00868-1.
[4] Sloan SW. Lower bound limit analysis using finite elements and linear programming. Int J Numer Anal Methods Geomech 1988;12:61–77. https://doi.org/10.1002/nag.1610120105.
[5] Liu F, Zhao J. Upper bound limit analysis using radial point interpolation meshless method and nonlinear programming. Int J Mech Sci 2013;70:26–38. https://doi.org/10.1016/j.ijmecsci.2013.01.017.
[6] Tin-Loi F, Ngo NS. Performance of a *p*-adaptive finite element method for shakedown analysis. Int J Mech Sci 2007;49:1166–78. https://doi.org/10.1016/j.ijmecsci.2007.02.004.
[7] Le VH, Tangaramvong S, Tran LV. Sequential elastic adaptive NS-FE analyses for lower-bound limit load determination of plane-strain structures. Int J Mech Sci 2021:205. https://doi.org/10.1016/j.ijmecsci.2021.106585.
[8] Ferradi MK, Fliscounakis A, Arquier M, Bleyer J. Elastoplastic and limit analysis of reinforced concrete with an equilibrium-based finite element formulation. Comput Struct 2023;286. https://doi.org/10.1016/j.compstruc.2023.107095.
[9] Fliscounakis A, Arquier M, Ferradi MK. 3D limit analysis of reinforced concrete with sliding along smeared cracks. Comput Struct 2024;305. https://doi.org/10.1016/j.compstruc.2024.107561.
[10] Kim YJ, Song TK, Kim JS, Jin TE. Limit loads and approximate *J* estimates for axial through-wall cracked pipe bends. Int J Fract 2007;146:249–64. https://doi.org/10.1007/s10704-007-9166-2.
[11] Lim K, Li AJ, Schmid A, Lyamin AV. Slope-stability assessments using finite-element limit-analysis methods. Int J Geomech 2017;17:1–8. https://doi.org/10.1061/(asce)gm.1943-5622.0000715.
[12] Zhou H, Wang Z, Liu H. Ultimate lateral pressure of circular pile in undrained clay considering the strength reduction induced by pile installation. Int J Geomech 2022;22:1–11. https://doi.org/10.1061/(asce)gm.1943-5622.0002323.
[13] Trentadue F, Quaranta G. Limit analysis of frictional block assemblies by means of fictitious associative-type contact interface laws. Int J Mech Sci 2013;70:140–5. https://doi.org/10.1016/j.ijmecsci.2013.02.012.

[14] Hua Y, Milani G. Simple modeling of reinforced masonry arches for associated and non-associated heterogeneous limit analysis. Comput Struct 2023;280. https://doi.org/10.1016/j.compstruc.2023.106987.
[15] Cavalagli N, Gusella V, Severini L. Lateral loads carrying capacity and minimum thickness of circular and pointed masonry arches. Int J Mech Sci 2016;115–116:645–56. https://doi.org/10.1016/j.ijmecsci.2016.07.015.
[16] Nodargi NA, Bisegna P. Collapse capacity of masonry domes under horizontal loads: a static limit analysis approach. Int J Mech Sci 2021;212. https://doi.org/10.1016/j.ijmecsci.2021.106827.
[17] Milani G. 3D FE limit analysis model for multi-layer masonry structures reinforced with FRP strips. Int J Mech Sci 2010;52:784–803. https://doi.org/10.1016/j.ijmecsci.2010.01.004.
[18] Izadi A, Ashouri Nalkiashari L, Payan M, Jamshidi Chenari R. Bearing capacity of shallow strip foundations on reinforced soil subjected to combined loading using upper bound theorem of finite element limit analysis and second-order cone programming. Comput Geotech 2023;160:105550. https://doi.org/10.1016/j.compgeo.2023.105550.
[19] Liao K, Wu Y, Miao F, Pan Y, Beer M. Quantitative risk assessment of seismically loaded slopes in spatially variable soils with depth-dependent strength. Int J Geomech 2024;24:04024113. https://doi.org/10.1061/IJGNAI.GMENG-9001.
[20] Yang XL, Zhang S. Stability analysis of 3D cracked slope reinforced with piles. Comput Geotech 2020;122:103544. https://doi.org/10.1016/j.compgeo.2020.103544.
[21] Gowtham G, Sahoo JP. Stability analysis of circular tunnels using spatiotemporal accelerations formulated considering heterogeneity of seismic wave propagation velocities. Soil Dyn Earthq Eng 2024;181:108654. https://doi.org/10.1016/j.soildyn.2024.108654.
[22] Yang F, Qin A, Zheng X, Yang J, Shiau J. Stability and failure mechanism of the tunnel face in nonhomogeneous clay with longitudinal slopes: a kinematic limit analysis. Int J Geomech 2024;24:1–15. https://doi.org/10.1061/ijgnai.gmeng-9782.
[23] van Huyssteen D, Rivarola FL, Etse G, Steinmann P. Quasi-optimal mesh generation for the virtual element method: a fully adaptive remeshing procedure. Comput Methods Appl Mech Eng 2025;435:117630. https://doi.org/10.1016/j.cma.2024.117630.
[24] Wiberg NE, Li XD, Abdulwahab F. Adaptive finite element procedures in elasticity and plasticity. Eng Comput 1996;12:120–41. https://doi.org/10.1007/BF01299397.
[25] Wang X, Zhang Y, Wen M, Mang HA. A simple hybrid linear and nonlinear interpolation finite element for the adaptive Cracking Elements method. Finite Elem Anal Des 2025;244:104295. https://doi.org/10.1016/j.finel.2024.104295.
[26] Wang C, Ping X, Wang X. An adaptive finite element method for crack propagation based on a multifunctional super singular element. Int J Mech Sci 2023;247:108191. https://doi.org/10.1016/j.ijmecsci.2023.108191.
[27] Ee KC, Dillon OW, Jawahir IS. Finite element modeling of residual stresses in machining induced by cutting using a tool with finite edge radius. Int J Mech Sci 2005;47:1611–28. https://doi.org/10.1016/j.ijmecsci.2005.06.001.
[28] Christiansen E, Pedersen OS. Automatic mesh refinement in limit analysis. Int J Numer Methods Eng 2001;50:1331–46. https://doi.org/10.1002/1097-0207(20010228)50:6<1331::AID−NME46>3.0.CO;2-S.
[29] Sun R, Yang J, Zhao Y, Liu S. Upper bound finite element limit analysis method with discontinuous quadratic displacement fields and remeshing in non-homogeneous clays. Arch Appl Mech 2021;91:1007–20. https://doi.org/10.1007/s00419-020-01806-z.
[30] Zhang J, Feng T, Yang J, Yang F, Gao Y. Upper-bound stability analysis of dual unlined horseshoe-shaped tunnels subjected to gravity. Comput Geotech 2018;97:103–10. https://doi.org/10.1016/j.compgeo.2018.01.006.
[31] Nguyen-Xuan H, Wu CT, Liu GR. An adaptive selective ES-FEM for plastic collapse analysis. Eur J Mech A Solids 2016;58:278–90. https://doi.org/10.1016/j.euromechsol.2016.02.005.
[32] Zhang J, Ding L, Liang Y, Zong J, Li Z. Upper-bound finite element adaptive analysis of plane strain heading in soil with a soft Upper layer and hard lower layer. Adv Civ Eng 2019:2019. https://doi.org/10.1155/2019/7387635.
[33] Zheng X, Yang F. An efficient and synchronous mesh refining-coarsening strategy in kinematic upper-bound limit analysis. Comput Geotech 2022;148:104843. https://doi.org/10.1016/j.compgeo.2022.104843.
[34] Muñoz JJ, Bonet J, Huerta A, Peraire J. Upper and lower bounds in limit analysis: adaptive meshing strategies and discontinuous loading. Int J Numer Methods Eng 2009;77:471–501. https://doi.org/10.1002/nme.2421.
[35] Zhang R, Li L, Zhao L, Tang G. An adaptive remeshing procedure for discontinuous finite element limit analysis. Int J Numer Methods Eng 2018;116:287–307. https://doi.org/10.1002/nme.5925.
[36] Sarvesh R, Srinivasan V, Patel A. Finite element limit analysis of the bearing capacity of an obliquely loaded strip footing on granular soil placed adjacent to vertically loaded existing footing. Geomech Eng 2023;35:287–306. https://doi.org/10.12989/gae.2023.35.3.287.
[37] Liao K, Wu Y, Miao F, Pan Y, Beer M. Probabilistic risk assessment of earth dams with spatially variable soil properties using random adaptive finite element limit analysis. Eng Comput 2023;39:3313–26. https://doi.org/10.1007/s00366-022-01752-0.
[38] Ali A, Lyamin AV, Huang J, Li JH, Cassidy MJ, Sloan SW. Probabilistic stability assessment using adaptive limit analysis and random fields. Acta Geotech 2017;12:937–48. https://doi.org/10.1007/s11440-016-0505-1.
[39] Lyamin AV, Sloan SW, Krabbenhøft K, Hjiaj M. Lower bound limit analysis with adaptive remeshing. Int J Numer Methods Eng 2005;63:1961–74. https://doi.org/10.1002/nme.1352.
[40] Borges L, Zouain N, Costa C, Feijóo R. Adaptive approach to limit analysis. Int J Solids Struct 2001;38:1707–20. https://doi.org/10.1016/S0020-7683(00)00131-1.
[41] Milani G, Lourenço PB. A discontinuous quasi-upper bound limit analysis approach with sequential linear programming mesh adaptation. Int J Mech Sci 2009;51:89–104. https://doi.org/10.1016/j.ijmecsci.2008.10.010.
[42] Lyamin AV, Kjrabbenhoft K, Sloan SW. Adaptive limit analysis using deviatoric fields. Adapt. Model. Simul. 2013 -. In: Proceedings of the 6th international conference on adaptive modeling and simulation, ADMOS 2013; 2013. p. 448–55.
[43] Kong D, Martin CM, Byrne BW. Modelling large plastic deformations of cohesive soils using sequential limit analysis. Int J Numer Anal Methods Geomech 2017;41:1781–806. https://doi.org/10.1002/nag.2700.
[44] Hua Y, Milani G. Novel continuous limit analysis modeling with deformable polygon discretization. Lect Notes Civ Eng 2024;460:153–63. https://doi.org/10.1007/978-981-97-0399-9_15. LNCE.
[45] Hussein A, Hudobivnik B, Wriggers P. A combined adaptive phase field and discrete cutting method for the prediction of crack paths. Comput Methods Appl Mech Eng 2020;372:113329. https://doi.org/10.1016/j.cma.2020.113329.
[46] Nguyen-Xuan H, Nguyen-Hoang S, Rabczuk T, Hackl K. A polytree-based adaptive approach to limit analysis of cracked structures. Comput Methods Appl Mech Eng 2017;313:1006–39. https://doi.org/10.1016/j.cma.2016.09.016.
[47] Ho PLH, Lee C. Adaptive quadtree edge-based smoothed finite element method for limit state analysis of structures. Int J Mech Mater Des 2024;20:1191–207. https://doi.org/10.1007/s10999-024-09716-6.
[48] Li M, Füssl J, Lukacevic M, Eberhardsteiner J, Martin CM. A numerical upper bound formulation with sensibly-arranged velocity discontinuities and orthotropic material strength behaviour. J Theor Appl Mech 2018;56:417–33. https://doi.org/10.15632/jtam-pl.56.2.417.
[49] Drucker DC. Coulomb friction, plasticity, and limit loads. J Appl Mech 1954;21:71–4. https://doi.org/10.1115/1.4010821.
[50] Ferris MC, Tin-Loi F. Limit analysis of frictional block assemblies as a mathematical program with complementarity constraints. Int J Mech Sci 2001;43:209–24. https://doi.org/10.1016/S0020-7403(99)00111-3.
[51] Y. Hua, G. Milani, Rigid block limit analysis of masonry arches with associated and non-associated slides, in: From corbel arches to double curvature vaults anal. conserv. restor. archit. herit. mason. struct., 2022: pp. 169–203. 10.1007/978-3-031-12873-8_7.
[52] Bottero A, Negre R, Pastor J, Turgeman S. Finite element method and limit analysis theory for soil mechanics problems. Comput Methods Appl Mech Eng 1980;22:131–49. https://doi.org/10.1016/0045-7825(80)90055-9.
[53] Cavicchi A, Gambarotta L. Two-dimensional finite element upper bound limit analysis of masonry bridges. Comput Struct 2006;84:2316–28. https://doi.org/10.1016/j.compstruc.2006.08.048.
[54] Cavicchi A, Gambarotta L. Collapse analysis of masonry bridges taking into account arch-fill interaction. Eng Struct 2005;27:605–15. https://doi.org/10.1016/j.engstruct.2004.12.002.
[55] Maier G, Nappi A. A theory of no-tension discretized structural systems. Eng Struct 1990;12:227–34. https://doi.org/10.1016/0141-0296(90)90021-J.
[56] Engwirda D. Locally-optimal delaunay-refinement and optimisation-based mesh generation. The University of Sydney; 2014.
[57] Prandtl L. Über die härte plastischer Körper, Nachrichten von Der Gesellschaft Der Wissenschaften Zu Göttingen. Math Klasse 1920;12:74–85.
[58] Aaron T. Becker's Robot Swarm lab, lloydsAlgorithm(Px,Py, crs, numIterations, showPlot), MATLAB Central File Exchange (2024). https://www.mathworks.com/matlabcentral/fileexchange/41507-lloydsalgorithm-px-py-crs-numiterations-showplot.
[59] Hua Y, Milani G. Novel block element with axial-only deformation for limit analysis of masonry arch bridges. Comput Struct 2024;298. https://doi.org/10.1016/j.compstruc.2024.107361.
[60] Drosopoulos GA, Stavroulakis GE, Massalas CV. Limit analysis of a single span masonry bridge with unilateral frictional contact interfaces. Eng Struct 2006. https://doi.org/10.1016/j.engstruct.2006.03.016.
[61] Betti M, Drosopoulos GA, Stavroulakis GE. Two non-linear finite element models developed for the assessment of failure of masonry arches. C R Mec 2008;336:42–53. https://doi.org/10.1016/j.crme.2007.10.014.
[62] Page J. Load tests to collapse on two arch bridges at preston, shropshire and prestwood, staffordshire. Res Rep Transp Road Res Lab 1987.
[63] Li M, Füssl J, Lukacevic M, Eberhardsteiner J, Martin CM. An algorithm for adaptive introduction and arrangement of velocity discontinuities within 3D finite-element-based upper bound limit analysis approaches. Comput Methods Appl Mech Eng 2019;348:875–911. https://doi.org/10.1016/j.cma.2018.12.017.